MSc Mechanical Engineering
Msc Report

# Active vibration damping of a sandwich beam using shear piezoelectric transducers

Kevin Nguyen

Committee: prof. dr. ir. W.B.J. Hakvoort, ir. B. Jansen, dr. ir. T. Esteves Rosa, dr. ir. J. Dasdemir, dr. ir. M. Feinaeugle

May , 2025

Chair of Control and Mechatronics
Department of Mechanics of Solids, Surfaces and Systems
Faculty of Engineering Technology,
University of Twente

UNIVERSITY OF TWENTE.

# NOMENCLATURE

| Abreviation | Definiton |
|---|---|
| ReMa | Reticle Masking Unit |
| PPF | Positive Position Feedback |
| EMCC | Electro-Mechanical Coupling Coefficient |
| $V_{\text{out}}$ | Voltage output of the shear piezo sensor |
| $V_{\text{in}}$ | Voltage input of the shear piezo actuator |
| $z_{\text{tip}}$ | Tip displacement of the cantilever beam |
| $f_{\text{base}}$ | Base actuation |

# CONTENTS

# Active vibration damping of a sandwich beam using shear piezoelectric transducers

Kevin Nguyen, Student Number: 2818965,
Control and Mechatronics, Mechanical Engineering,
University of Twente
Supervisors: prof. dr. ir. W.B.J. Hakvoort, ir. B. Jansen, dr. ir. T. Esteves Rosa

***Abstract*—The Reticle Mask (ReMa) blade is an essential component of the lithography machine for producing integrated circuits. This study focuses on the ReMa x-blade, which can be considered as a cantilever beam. The beam is subjected to high acceleration, inducing parasitic vibrations. The objective of this project is to suppress these parasitic vibrations using shear piezoelectric transducers. The shear piezoelectric elements are embedded within a sandwich-structured beam with sidewalls included to isolate the piezoelectric elements from external conditions. The optimal piezo configuration for this system is determined through numerical analysis of the system's transverse displacement and electromechanical Coupling Coefficient (EMCC). This research investigates two piezo configurations: a non-collocated piezo configuration and a collocated piezo configuration. Based on the numerically identified optimal piezo configuration, prototype designs are manufactured. Although the prototype design does not have sidewalls, it is designed to replicate the system behavior with sidewalls included. The open-loop identification is performed on the prototype systems, and an optimal positive position feedback (PPF) controller method is implemented to suppress the parasitic vibration. This controller provides significant damping for both non-collocated and collocated systems.**

***Index Terms*—ReMa blade, parasitic vibrations, piezoelectric, suppress, optimal piezo configuration, Positive Position Feedback**

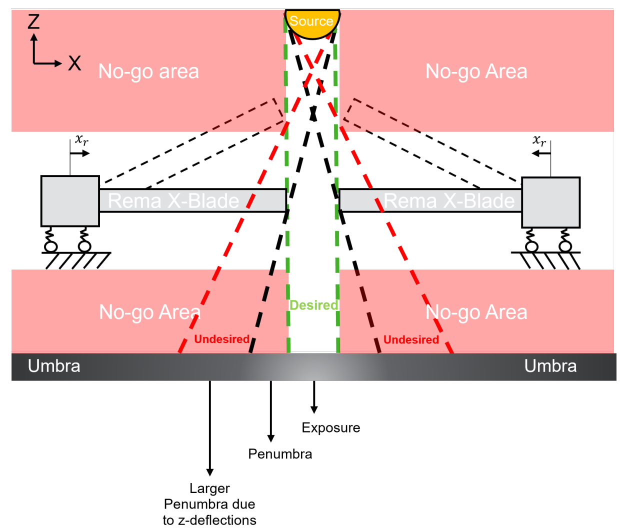


Fig. 1: The ReMa x-blade is fixed to the block and it moves in the x-direction ($x_{\mathrm{r}}$) to mask and expose the incoming light. However, due to high acceleration in $x_{\mathrm{r}}$, z-vibrations are induced and some unwanted light will pass through the mask.

## I. Introduction

### A. Background

The demand for more computing power and smaller integrated circuits or chips has increased throughout the years. One of the critical steps in producing integrated circuits is conducted by a lithography machine. The subcomponents of this machine, specifically the wafer and the Reticle Mask (ReMa), operate under high acceleration, which is essential for producing powerful and smaller integrated circuits [1]. However, the drawback of using high acceleration is that it induces parasitic vibrations in the subcomponents, negatively impacting the machine's performance [2]. This paper focuses on the ReMa x-blade, which can be considered as a cantilever beam, as illustrated in Figure 1. In the lithography machine, the light source and the ReMa blade are utilized to create patterns on the wafer. The purpose of the ReMa blade is to move at high acceleration along the x-axis to block and expose the incoming light, thereby creating patterns on the wafer. The main issue is that the high acceleration in the x-axis induces parasitic vibrations in the z-axis, moving the beam into the no-go area. As seen in Figure 1, unwanted light passes through the mask due to parasitic vibrations, leading to lower production quality of the integrated circuit. The maximum amplitude of parasitic vibrations that has been registered is $400\mu$m in the z-axis, caused by partly quasi-static and dynamic effects. A potential solution to reduce thermal deformations is by implementing a water-cooling system. To reduce the dynamic effects, Abdelmoeti et al. [8] proposed placing extended piezoelectric elements on the beam's surface with different controller methods. His research showed potential in suppressing parasitic vibrations. However, placing the patches on the beam's surface adds external volume to the system, which is undesirable due to limitation on the design volume. Additionally, the piezoelectric transducers might be sensitive to external conditions, which could impact their performance. This problem could be solved by placing the piezoelectric elements inside the beam. The internal placement requires a different piezoelectric transducer than the conventional extensional piezoelectric transducers. The extensional transducers depend on modal bending strain normal to the cross-section; however, the bending strain decreases towards zero near the neutral line. Therefore, for the internal placement of the transducers, shear piezoelectric transducers are a potential alternative to drive the system. Baken et al. [3] investigated the integration of shear piezoelectric transducers within the beam to suppress parasitic vibrations. His research focused on a sandwich structure beam with a core layer composed of foam and integrated piezoelectric transducers. A PPF controller was utilized to suppress the parasitic vibrations. His findings indicated where to optimally place the transducers, and the transfer function of the open-loop system was obtained. Nevertheless, he was not able to demonstrate active vibration damping.

### B. Design and control goals

This research continues the work of Baken et al. [3], with the main goal of further developing his shear piezo-based beam system through a proof-of-concept beam that more closely represents the ReMa blade system capable of suppressing parasitic vibrations. To achieve the main goal of this research, the goal is divided into multiple subgoals.

*1) Develop a conceptual design with sidewalls using the same dimensions as the current ReMa blade beam:* Baken et al. [3] developed a sandwich beam with the sides still exposed to external conditions. However, in the final application, the sides must be enclosed to isolate the piezoelectric transducers from the external environment. Additionally, a water-cooling system will be implemented in future research to address the quasi-static issue. This system also requires sidewalls to prevent water leakage. In this subgoal, simulations will be performed to investigate the development of a beam system that includes sidewalls. The sandwich beam with sidewalls is illustrated in Figure 2.

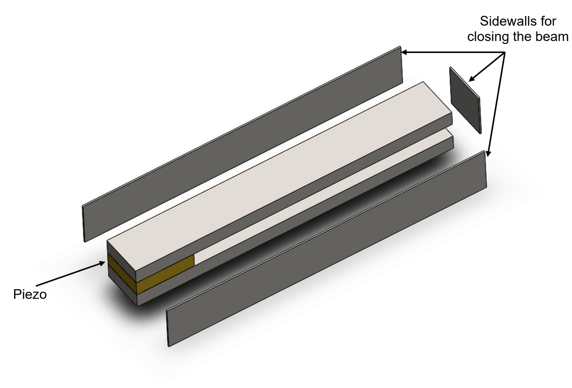


Fig. 2: A cantilever beam fully enclosed with sidewalls with one open side. This open side is used for clamping.

The new ReMa blade design should not differ much in dimensions from the current ReMa Blade design, see Table I.

*2) Develop a prototype design that replicates the dynamic behavior of the design with sidewalls.:* Sidewalls are not included in the experimental design to avoid further manufacturing issues. Nevertheless, a system is developed that replicates the dynamic behavior of a system with sidewalls.

TABLE I: ReMa x-blade Dimensions

| parameter | Value | Unit |
|---|---|---|
| L | 219 | [mm] |
| W | 32 | [mm] |
| H | 2.5 | [mm] |

This approach provides a meaningful starting point for understanding and predicting the behavior of a system with sidewalls.

*3) Design a system capable of counteracting $400\mu m$ vibrations for the first fundamental mode:* As mentioned previously, the current ReMa x-blade is exposed to a maximum of $400\mu$m parasitic vibrations. Therefore, a beam must be developed that is capable of counteracting the vibrations without saturating the system. This system can be considered as a cantilever beam with base disturbance. Figure 3 shows a COMSOL simulation of the maximum transverse (parasitic) displacement resulting from base excitations over the frequency range up to $1000Hz$.

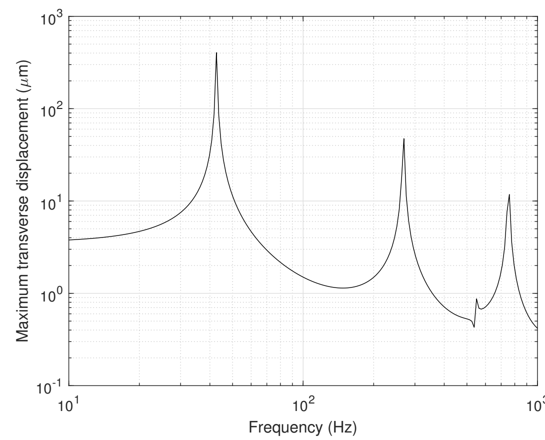


Fig. 3: The COMSOL simulation plot shows the maximum transverse displacement resulting from base excitations over the frequency range up to $1000Hz$

This figure illustrates the low-pass behavior of the system and indicates that the first mode contributes the highest parasitic vibrations. Consequently, the goal is to develop a system capable of counteracting $400\mu$m amplitude for the first fundamental mode.

*4) Achieve effective damping control for the first fundamental mode:* When a system is developed that is capable of counteracting $400\mu$m parasitic vibrations for the first fundamental mode, a controller must be implemented to suppress this mode. Therefore, the final goal is to implement a controller that can achieve effective damping control for the first fundamental mode.

### C. Literature

The research conducted by Baken et al. [3] utilizes the electromechanical coupling coefficient (EMCC) to determine the optimal piezo configuration. This approach is suggested and employed by Trindade et al. [6]. Additionally, Zhang and Sun et al. [5] have investigated shear mode piezoelectric actuators to produce transverse deflections in a sandwich structure. Their study focuses on the effect of actuator position and length on actuation performance. These prior studies are conducted on a sandwich beam using foam as the core layer. However, the end application of the ReMa blade will not include foam, and the sides of the sandwich structure must be enclosed. Consequently, the research gap is that the current research does not address the performance of piezoelectric configurations in systems with higher stiffness or those that include sidewalls to enclose the sandwich structure, as opposed to systems using foam core layers with open sides. Therefore, this research will contribute by analyzing the design of a shear piezo-based beam that includes sidewalls instead of foam, and by demonstrating active control damping through a proof-of-concept design.

### D. Outline

The next section elaborates on the methods employed to obtain the piezo configuration. Following this, simulations are conducted to determine the optimal piezo configuration. In section 4, the controller method will be discussed. Thereafter, the materials and experimental design are explained. Section 6 presents the results derived from the experimental measurements. Section 7 discusses the conclusion and section 8 provides recommendation and future steps.

## II. Piezo configuration method

This section discusses methods for obtaining the optimal piezo configuration in the ReMa blade to suppress parasitic vibrations. "Optimal" is defined as having the piezoelectric transducer configuration such that actuation and sensing performance are most effective for counteracting parasitic vibrations. The first optimal piezo configuration method discusses the utilization of transverse displacement of the beam caused by shearing, which is suggested by Zhang and Sun et al. [5]. The second method discusses the Electromechanical Coupling Coefficient (EMCC) to identify the optimal piezo configuration, suggested by Trindade et al. [6].

### A. Optimizing based on transverse displacement

Shear piezoelectric transducers generate or sense shear deformations. Embedding these transducers into a cantilever beam will induce transverse displacements of the system or sense shear deformations from the transverse displacement. Hence, Zhang and Sun et al. [5] suggest considering transverse displacement as a criterion for selecting the optimal piezo configuration in the beam. This is achieved by varying the piezoelectric element position and length to determine the most effective piezo configuration for counteracting parasitic vibrations.

### B. Electromechanical Coupling Coefficient

Electromechanical Coupling Coefficient (EMCC) is suggested as an optimization criterion for piezoelectric elements positioning and sizing inside the cantilever beam [6]. EMCC defines the effective energy conversion ($U_{\text{conv}}$) from the mechanical to the electrical domain, or vice versa, from the total energy ($U_{\text{tot}}$) stored in the piezoelectric element.

$$k^2 = \frac{U_{\text{conv}}}{U_{\text{tot}}} \tag{1}$$

Moreover, EMCC is also utilized as an important parameter for various applications, such as active control improvement [6]. The EMCC coefficient can be determined by evaluating the system under open and short circuit conditions. In open-circuit measurement, a branch of the circuit is left open, preventing current from flowing through it. In this measurement, both mechanical and electrical energy are stored in the piezoelectric body. A short circuit test is conducted by intentionally shorting a part of the circuit. This measurement allows the system's current to be measured while the voltage is low. During the short circuit analysis, the piezoelectric body will only perform mechanical energy. Hence, using the energy from the open circuit ($U_{\text{oc}}$) and short circuit ($U_{\text{sc}}$), equation (1) can also be described as:

$$k^2 = \frac{U_{\text{conv}}}{U_{\text{tot}}} = \frac{U_{\text{oc}} - U_{\text{sc}}}{U_{\text{oc}}} = \frac{w_{\text{oc}}^2 - w_{\text{sc}}^2}{w_{\text{oc}}^2} \tag{2}$$

$U_{\text{oc}}$ and $U_{\text{sc}}$ include similar terms, which can be neglected, allowing the equation to be further simplified into the open circuit frequency ($\omega_{\text{oc}}$) and short circuit frequency ($\omega_{\text{sc}}$). An alternative way of determining the EMCC is to evaluate the impedance of the system [7]. The resonance of the impedance defines work done by the mechanical domain, and the anti-resonance defines work done by the electrical and mechanical domains. Hence, using the resonance frequency ($\omega_{\text{a}}$) and anti-resonance frequency ($\omega_{\text{r}}$), equation (2) can also be defined as:

$$k^2 = \frac{\omega_{\text{a}}^2 - \omega_{\text{r}}^2}{\omega_{\text{a}}^2} \tag{3}$$

In the next section, simulations with COMSOL are conducted to determine the optimal piezo configuration. Given that impedance can be conveniently obtained in COMSOL, equation (3) is employed to evaluate the EMCC.

## III. Optimal piezo configuration

This section discusses the beam design with and without sidewalls and identifies the piezo configuration that meets the design goals. The optimal piezo configuration is determined through COMSOL simulations, based on the methods discussed in section II. The primary objective of this section is to design a system with sidewalls. The system without sidewalls is utilized for experimentation and needs to replicate the dynamic behavior of the system with sidewalls. The model with sidewalls for COMSOL is based on the 3D model as shown in Figure 2. For the model without sidewalls, see Figure 4.

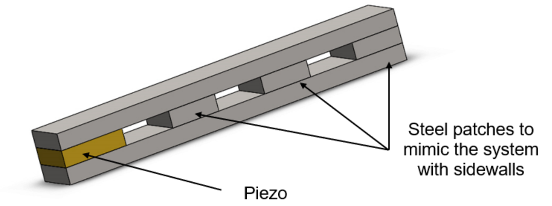


Fig. 4: A side view of the system with the sides open. The steel patches in the core layer are utilized to replicate the dynamic behavior of the system with sidewalls.

This model has three steel patches embedded in the core layer, each measuring 30mm in length. One patch is located at the free end, while the remaining two are placed next to each other with a 30mm spacing between each patch. This design allows for a close resemblance with the system with sidewalls. The other model properties for both systems are shown in Table II. The table presents the thickness of the core

TABLE II: COMSOL design properties

| Model properties | data |
|---|---|
| Thickness steel plates ($t_s$) | 1[mm] |
| Core thickness ($t_c$) | 0.5[mm] |
| Sidewall thickness ($t_w$) | 1[mm] |
| Piezo Material | PZT-A5 |
| Density steel ($\rho$) | 7800[kg/m$^3$] |
| Young's modulus steel ($E$) | 200GPa |
| Poisson's ratio steel ($\nu$) | 0.3 |
| Isotropic loss factor ($\eta$) | 0.01 |

layer and the upper and lower steel plates for both systems. It also specifies the sidewall thickness for the system with sidewalls and the piezoelectric material utilized in COMSOL simulations. Material damping is defined using the isotropic loss factor. This value is chosen manually and cannot be precisely determined without experimental testing. For further analysis an isotropic loss factor of $1\%$ is chosen.

## A. *Piezo Actuator configuration*

The first step is to identify the optimal placement and length of the piezoelectric actuator. This is required to achieve the optimal performance of the actuator to counteract $400\mu$m parasitic vibrations. Figure 5 presents a schematic representation of what parameters need to be varied in COMSOL simulations.

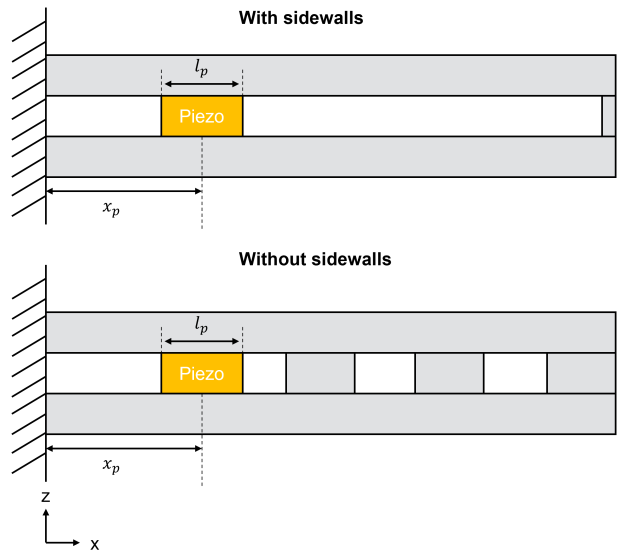


Fig. 5: A side view of the system with and without sidewalls. The system vibrations are induced in the z-axis

The first parameter investigated is the actuator's position. Method II-A is analyzed first. In this method, the position of a 10mm long piezoelectric element is varied along the beam. At each point along the beam length, the transverse displacement is measured at the resonance frequency for the first three fundamental modes. The results are shown in Figure 6.

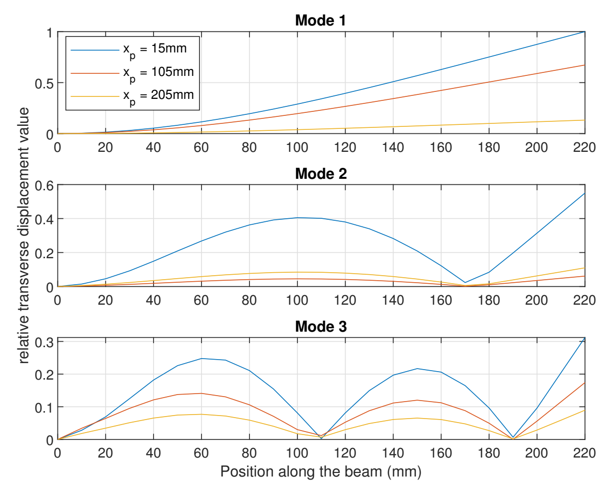


Fig. 6: Transverse displacement of the beam with sidewalls with varied actuator performances for each mode. The displacement values are all relative to the maximum displacement value of the first mode from the system with the actuator positioned at $x_p = 15$mm

This figure illustrates the results of the system with sidewalls, highlighting the different actuation performances for each mode. The system without sidewalls gives similar results. The shape of each mode remains unchanged, but only the amplitude varies. The beam's tip exhibits the highest displacement for each mode. Therefore, the tip is analyzed further. The average frequencies over the actuator positions of each mode are shown in Table III.

TABLE III: Natural frequencies

| | With Sidewalls | No Sidewalls | Baken's Beam |
|---|---|---|---|
| Mode 1 | 46.4 | 42.6 | 27.2 |
| Mode 2 | 281.7 | 227.3 | 142 |
| Mode 3 | 753.7 | 589.1 | 338 |

The design without sidewalls is utilized for experimentation and needs to replicate the dynamic behavior of the system with sidewalls. The embedded steel patches increase the stiffness of the core layer, thereby aligning more closely with the resonance frequencies of the system with the sidewalls. When comparing these systems with Baken's beam, a significant difference in frequency is observed. This is due to Baken's beam using foam in the core layer, making the system less stiff and consequently lowering the natural frequencies. Appendix F provides a detailed illustration of Baken's beam. In the final application of the ReMa blade, no foam will be utilized. Therefore, the dynamics of the current beams provide a better representation of the ReMa blade system.

Figure 7 depicts the result of the tip displacement at resonance frequency for the first three modes against actuator position.

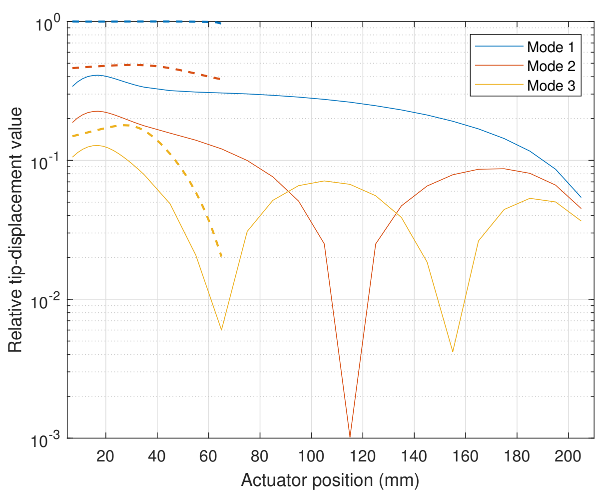


Fig. 7: Tip displacement against actuator position. The dashed line represents the beam with no sidewalls included. The output values are all relative to the maximum value of the system with the highest actuation performance.

The results of both systems are shown. The system without sidewalls can only be observed until $x_\mathrm{p} = 65$mm due to the steel patches. The optimal actuator placement for both systems is found near the fixed end. Both systems exhibit similar behavior until $x_\mathrm{p} = 65$mm, but the system without sidewalls has a higher coupling than the system with sidewalls. The system with sidewalls has a lower coupling due to the additional sidewalls, which add extra mass and constraint to the system.

When observing the system with sidewalls, notice that the effective performance of the actuator is located near the fixed end and around the node points of each mode shape. Additionally, the observed dips with low transfer correspond to the anti-node points of the mode shape. These behaviors are due to the high reaction stress occurring near the fixed end, and at node points during bending, and low stress at anti-node points. See Appendix E for details on how shear stresses affect the system's performance.

The next evaluation criterion involves evaluating the Electromechanical Coupling Coefficient (EMCC). The EMCC is obtained by analyzing the system's impedance and using Equation 3. Figure 8 depicts the EMCC values against the actuator position for the second and third modes. The EMCC for the first mode could not be plotted because COMSOL could not achieve an accurate EMCC plot. However, it is expected that the first mode is placed lower than the second mode and exhibits similar behavior to the first mode in Figure 7.

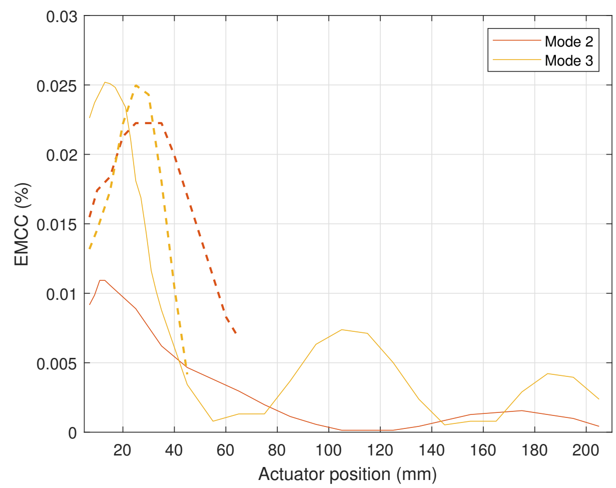


Fig. 8: EMCC values against the actuator position with a piezoelectric element length of 10mm. The dashed line represents the beam with no sidewalls included

The results show similar behavior to the results from the transverse displacement criterion. The main difference is that this figure exhibits wider dips. Furthermore, this graph indicates higher EMCC coupling for higher modes. According to the EMCC values, the highest performance is near the fixed end for both systems. For the system without sidewalls, it shows a higher EMCC performance than the system with sidewalls, also due to lower overall stiffness of the system. However, this system experiences a significant EMCC drop when moving from 25mm towards the fixed end.

Additionally, the results of both systems show different behavior compared to the EMCC figure from Baken's beam. In Baken's system, the optimal placement is at 38.8mm, and performance decreases significantly when moving towards the fixed end. This is attributed to the low stiffness of the system.

The next analysis involves varying the length to evaluate the actuation performance. In the final application, the sidewalls will be implemented into the system. From the transverse displacement and EMCC method, it is evident that the optimal placement is near the fixed end. Therefore, for the next analysis of varying the sensor length along the beam's length, the piezoelectric actuator will be placed at the fixed end. Figure 9 depicts the result of the tip displacement against the actuator length.

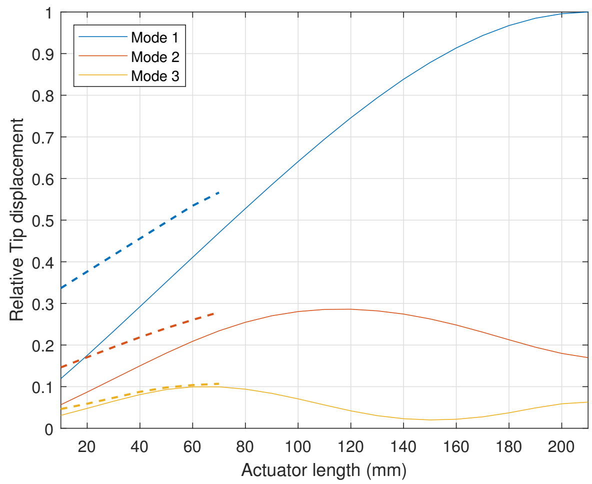


Fig. 9: Tip displacement against actuator length, with the values relative to the maximum displacement of the first mode from the system with sidewalls. The dashed line represents the beam with no sidewalls included

The points where high reaction stresses can be found during bending also explain the behavior of this figure. For the first mode, the performance increases consistently with actuator length. For the other modes, performance increases up to an anti-node point of the mode shape, and after that, performance will decrease. Assuming the shear piezoelectric element with a thickness of 0.5mm has an electric field of 500V/mm. The actuator length for the system with sidewalls needs to be at least 30mm to achieve 400$\mu$m tip vibrations for the first mode without becoming saturated. This holds true if the isotropic loss factor of the system is 0.01.

Figure 10 depicts the result of the EMCC plotted against the actuator length. This graph also shows higher EMCC values for higher modes, and the shape behavior for each mode is similar to Figure 9 for both systems. For the next analysis, an actuator length of 30mm is utilized.

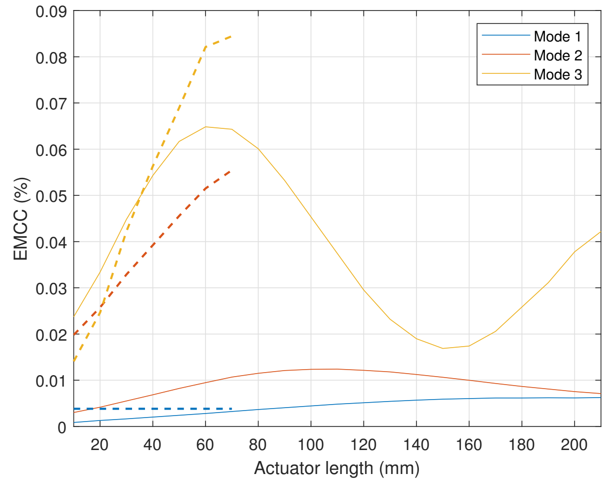


Fig. 10: EMCC value against actuator length. The dashed line represents the beam with no sidewalls included.

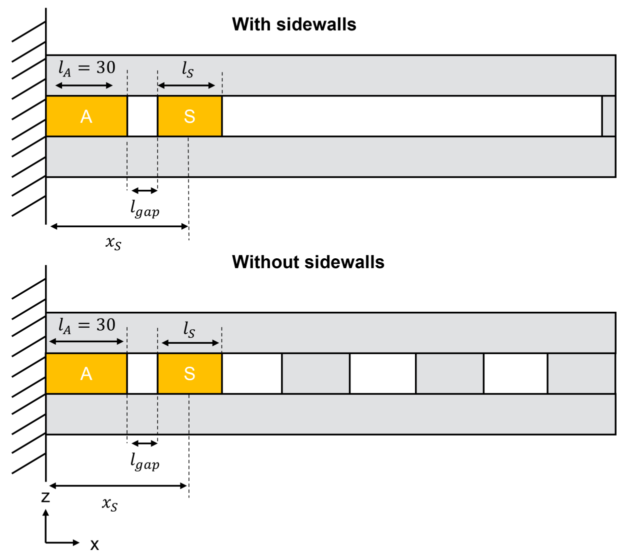


Fig. 11: a non-collocated actuator sensor design in (mm) with vibrations induced in the z-axis

## B. Sensor configuration for a Non-Collocated design

A sensor is required to detect unwanted vibrations. These vibrations are fed back to the controller and actuator for counter-actuation. This subsection discusses the placement of the sensor next to the actuator, resulting in a non-collocated system, as shown in Figure 11. The parameters in this figure are varied to obtain the optimal coupling between the sensor output and actuator input. High coupling enables better output readings from the sensor. Figure 12 depicts the results of the output of the sensor with a length of 10mm as a function of actuator position.

The result of both systems shows similar behavior. The system without sidewalls has a higher coupling, which is also due to lower stiffness compared to the system with sidewalls. When observing the behavior of the system with sidewalls, it also depicts high coupling around node points and near the actuator. This is because the piezoelectric sensor reads shear stresses, which are the highest near the fixed end and at node points of the mode shape. See Appendix E to see the shearstress analysis. Moreover, for effective control implementation, it is ideal to position the sensor next to the actuator to achieve near-collocated behavior. A fully collocated system, characterized by alternating poles and zeros, ensures closed-loop stability [9]. Nevertheless, placing the sensor directly against the actuator is not ideal because the sensor will read both bending stresses and local stresses from the actuator. These combined stresses lead to a significant increase in coupling between actuator and sensor. The effects of this can be seen in Figure 12, particularly for the first mode. Figure 13 depicts different bodeplots of various sensor positions for the

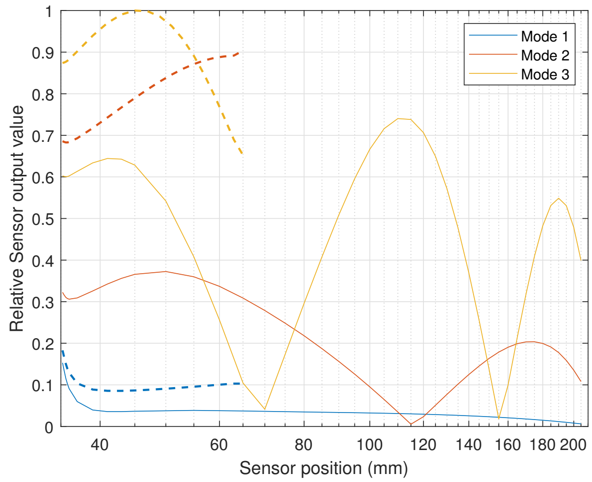


Fig. 12: The sensor output is plotted against the sensor position, with the output values relative to the maximum output from the system without sidewalls. The dashed line represents the beam configuration with no sidewalls.

system with sidewalls.

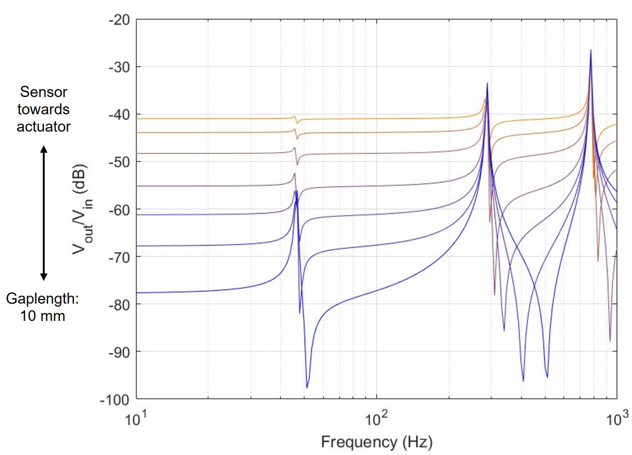


Fig. 13: $V_{\mathrm{out}}/V_{\mathrm{in}}$ Bodeplots of different sensor positions for the system with sidewalls

The figure illustrates that as the sensor moves closer to the actuator, the DC-value increases significantly. This behavior is also observed in the system without sidewalls. However, the increase in the DC-value also reduces the peak resonance height and brings the poles and zeros closer together. Achievable control damping depends on the spacing between poles and zeros [14]. Closely spaced poles and zeros limit control damping. Therefore, the actuator and the sensor need to be decoupled as much as possible to ensure that the sensor primarily detects the stresses induced by bending. Consequently, a sensor position needs to be identified where the DC-value is minimized. This also results in wider spacing between the poles and zeros, as shown in Figure 13. Figure 14 depicts the DC value of $V_{\mathrm{out}}/V_{\mathrm{in}}$ against the gap length ($l_{\mathrm{gap}}$) between the actuator and the sensor. The results of the system with

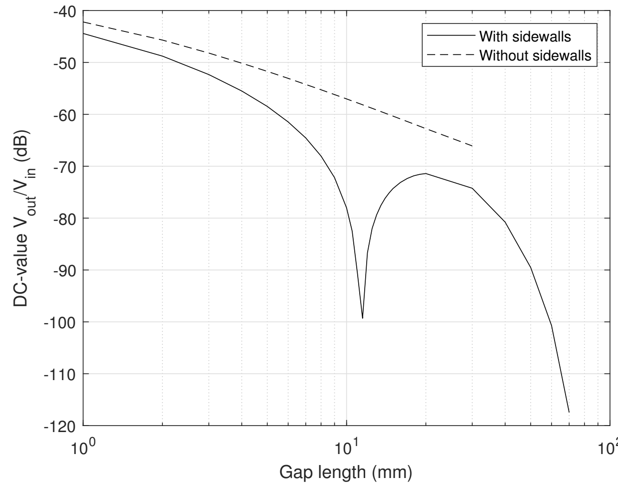


Fig. 14: DC value of $V_{\mathrm{out}}/V_{\mathrm{in}}$ against the gaplength between actuator and the sensor

sidewalls show a minimum, whereas the other system does not. The left side of the minimum depicts the bodeplots, as shown in Figure 13. The right side of the minimum introduces another antiresonance before the first mode resonance, as shown in Figure 15. This behavior could be attributed to the additional

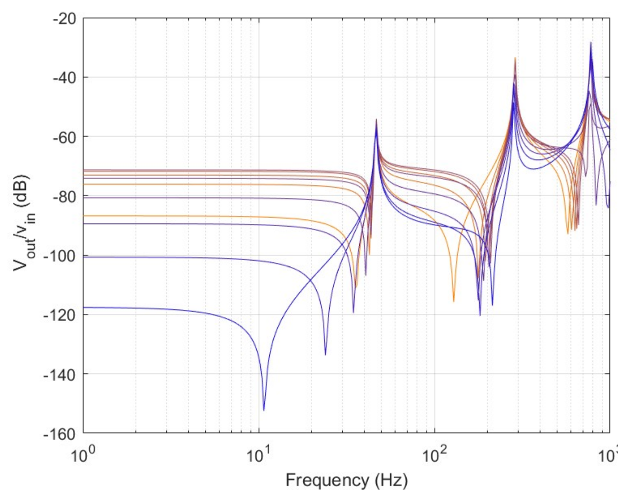


Fig. 15: multiple bodeplots for varying gap length ($l_{\mathrm{gap}}$) starting from yellow 12mm to blue 20mm

mass and constraint from the sidewalls. Moreover, as shown in this figure, when moving the sensor further away from the actuator, the system behavior begins to exhibit high-pass behavior. This phenomenon makes sense because the shear piezoelectric sensor detects shear stresses, which are related to acceleration. Consequently, the shear piezoelectric sensor can be considered an accelerometer. At higher frequencies, rapid changes in shear strains result in higher derivatives of shear strains, leading to higher accelerations. Conversely, lower frequencies exhibit slower changes in strain, resulting in lower derivatives and thus lower accelerations. Hence, the shear piezoelectric sensors exhibit high-pass behavior.

In this project, it has not been further analyzed whether this antiresonance has a positive or negative influence on control implementation. Nevertheless, to achieve a more collocated behavior, $l_{\text{gap}}$ needs to be as small as possible without having significant local stress readings from the actuator. Therefore, the left side of the minimum is taken for choosing $l_{\text{gap}}$. To minimize the local stress readings from the actuator, a gap length of 10mm is chosen.

Another parameter that needs to be considered in the design is the length of the sensor. Figure 16 shows the bodeplots of multiple sensor lengths for both systems with and without sidewalls. In a case with sidewalls, the poles and zeros become more widely spaced, particularly for the first mode. Therefore, increasing the sensor length will enhance control damping. However, the system will also become less collocated, which complicates control implementation. In the system without sidewalls, there is lower coupling with increasing length, and the resonance and antiresonance of each mode do not widen significantly. The prototype design without sidewalls, which will be discussed in the next section, cannot validate whether the system improves further by increasing the sensor length. Therefore, the sensor length of 10mm is chosen for both systems to aim for better near-collocated behavior. Additionally, the poles and zeros of the first mode of both systems are closely spaced. Therefore, experiments will be performed to determine if effective control damping can be achieved for a system with closely spaced poles and zeros.

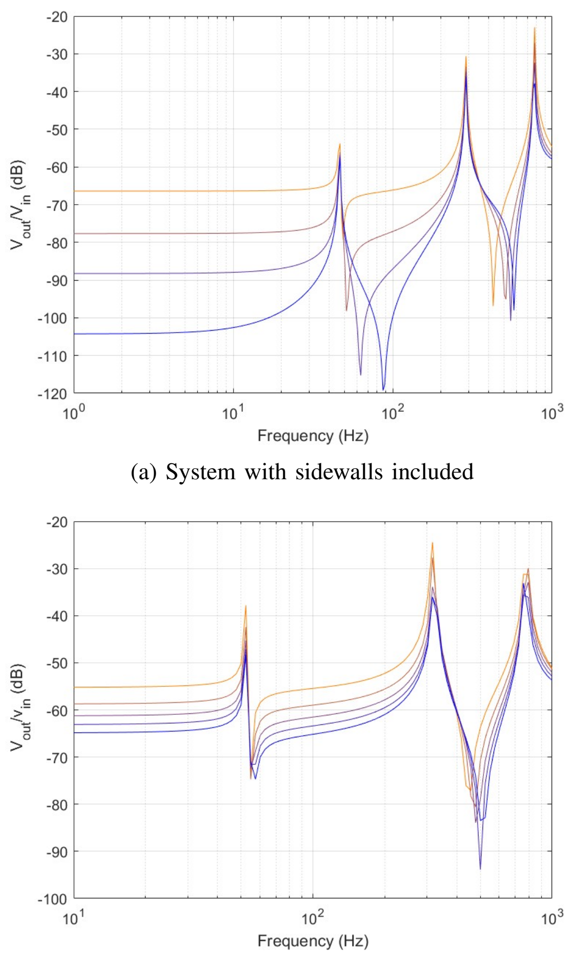


(a) System with sidewalls included

(b) System without sidewalls included

Fig. 16: Bodeplots of multiple variable sensor length for a system without sidewalls starting from yellow 5mm to blue 20mm

## C. Collocated design configuration

An alternative design approach involves employing the method of structured electrodes by positioning the sensor between two actuators and removing the electrodes between them. This configuration enables the system to actuate and sense in a fully collocated manner, as illustrated in Figure 17.

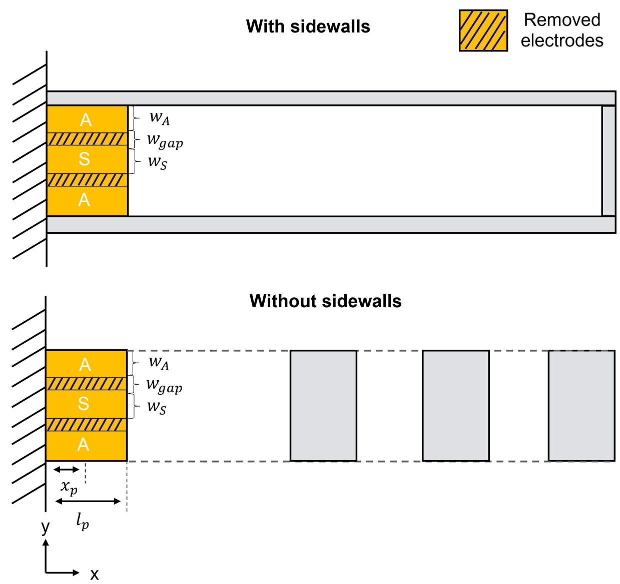


Fig. 17: A top view of the core layer. This system represents a collocated design.

Having a fully collocated design ensures a stable control system. This design eliminates the electrode spacing between the actuator and the sensor, allowing for actuation and sensing within a single piezoelectric element. In the optimal piezo configuration, the sensor needs to be as small as possible, while the actuator should be as wide as possible to achieve the best actuation performance. To maintain connectivity for electrical wiring, the sensor width is set at 2mm. Ideally the actuator should be as wide as possible. However, the sensor in the collocated design will also experience local stresses from the closely distant actuator. Hence, another static analysis is conducted to determine which actuator width minimizes local stresses on the sensor while being wide enough to meet the requirement of counteracting $400\mu$m. Figure 18 depicts the DC-value of $V_{\text{out}}/V_{\text{in}}$ against the actuator width. Similar to Figure 14, the static behavior has a minimum and this time also for both systems. On the left side, the system also introduces an antiresonance before the first mode resonance, see Appendix B. On the right side, the system does not have the antiresonance before the first mode resonance. The chosen

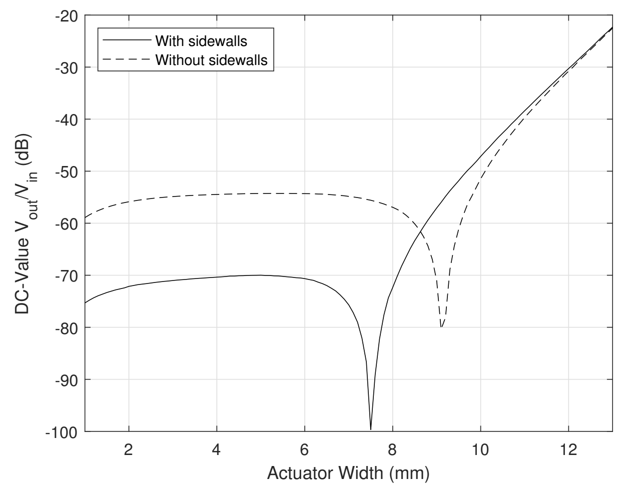


Fig. 18: DC value of $V_{\text{out}}/V_{\text{in}}$ against actuator width

actuator width needs to be as wide as possible but also small enough such that the sensor experiences minimal local stresses from the actuator. Therefore, the actuator width between 7.5 and 13mm for the system with sidewalls is further analyzed. Figure 19 depicts several bodeplots of different actuator width and gives a better overview of finding the optimal actuator width. The system with an actuator width greater than 8mm

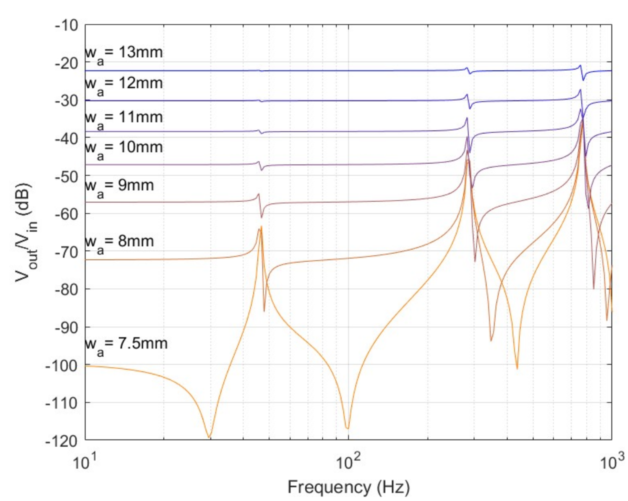


Fig. 19: $V_{\text{out}}/V_{\text{in}}$ Bodeplots of $w_a$ between 7.5 and 13mm

exhibits high coupling with low resonance peak height. This is attributed to increased local stress readings. Therefore, an actuator width between 7.5 and 8mm would be optimal regarding control implementation. For the final design with sidewalls, an actuator width of 8mm is chosen to achieve better actuation performance. With a similar approach for the system without sidewalls, the actuator width between 9 and 10mm would be taken for further analysis.

### *D. Final conceptual design*

This subsection summarizes the final design for the non-collocated and collocated systems with sidewalls, based on the findings from the previous subsections. The designs are derived from the ReMa blade dimensions in Table I and the thickness dimensions in Table II. The length of the piezo actuator cannot yet be specified because the damping properties are not known and need to be determined experimentally. The identified parameters for the non-collocated and collocated designs are presented in Table IV and Table V.

TABLE IV: Final design Non-collocated system

| parameter | value [mm] |
|---|---|
| $x_A$ | $l_A/2$ (fixed end) |
| $l_A$ | - |
| $l_{gap}$ | 10 |
| $l_S$ | 10 |

TABLE V: Final design Collocated system

| parameter | value [mm] |
|---|---|
| $x_{\text{p}}$ | $l_p/2$ (fixed end) |
| $l_{\text{p}}$ | - |
| $w_{\text{A}}$ | 8 |
| $w_{\text{gap}}$ | 10 |
| $w_{\text{S}}$ | 2 |

The design without sidewalls discussed in the previous subsection shows that it provides a good representation of the system with sidewalls and serves as a good starting point for understanding and predicting the dynamic behavior of the system with sidewalls. The prototype design without sidewalls will be discussed in the next section.

## IV. Control method

To suppress the parasitic vibrations in the system, a sensor is required to detect them and provide feedback to an active vibration controller and actuator to counteract them. Figure 20 depicts the control scheme for this system. $w$ is the

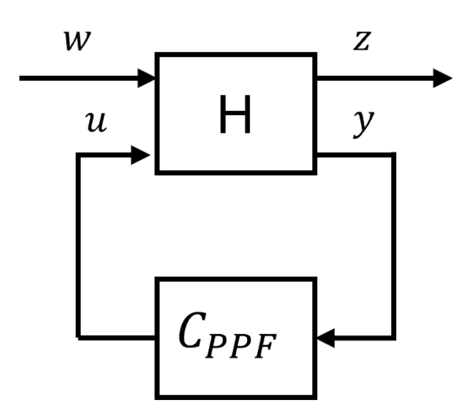


Fig. 20: Control scheme of a beam with an active vibration controller

disturbance, and a control loop is implemented between sensor output $y$ and actuator input $u$ to suppress the signals within the performance channel $z$. Consequently, a multiple-input and multiple-output (MIMO) system is represented.

### A. Positive Position Feedback controller

One of the design goals is to suppress the first fundamental mode of the parasitic vibrations. Baken et al. [3] proposed the utilization of a Positive Position Feedback (PPF) controller, a common method for systems with piezoelectric actuators. This resonant controller, introduced by Goh [10], is designed to suppress targeted modes without changing the overall structural behavior. The controller can be described as:

$$C_{PPF} = \frac{k\omega_c^2}{s^2 + 2\zeta_c\omega_c s + \omega_c^2} \tag{4}$$

$k$ is the gain, $\omega_c$ is the controller resonance frequency, and $\zeta_c$ is the controller damping ratio. These parameters need to be tuned to achieve the desired damping of the targeted mode.

### B. Optimal Tuning Method

Finding the optimal parameter values can be achieved through an optimal tuning method. Most developed tuning methods assume that the system can be reduced to a single mass spring system that exhibits roll-off after the targeted resonance [4]. Nevertheless, this assumption is in general not valid as the response may also be influenced by higher frequency dynamics [4].

Seinhorst et al. [4] investigated an $H_2$ and $H_\infty$ optimal tuning problem of PPF controllers for a general class of systems. His research demonstrated that the system can be simplified into a single mass spring system. However, additional direct feedthrough terms need to be considered which represents the effect of the higher frequency dynamics. With these terms included and utilizing the $H_2$ and $H_\infty$ norms to minimize the closed-loop transfer from $z$ to $w$ , his optimal tuning method showed effective result in active vibration damping. The optimal tuning process begins by defining the high- and low-frequency asymptotes of the targeted mode. This is conducted by representing the whole system in a modal state-space form and subsequently reducing it to:

$$\begin{aligned} \ddot{\eta} + \omega_n^2\eta &= \begin{bmatrix} b_w & b_u \end{bmatrix} \begin{bmatrix} w \\ u \end{bmatrix}, \\ \begin{bmatrix} z \\ y \end{bmatrix} &= \begin{bmatrix} f_z \\ f_y \end{bmatrix} \eta + \begin{bmatrix} d_{zw} & d_{zu} \\ d_{yw} & d_{yu} \end{bmatrix} \begin{bmatrix} w \\ u \end{bmatrix} \end{aligned} \tag{5}$$

$\omega_n$ represents the natural frequency, $\eta$ the modal coordinates, $b$ the input terms, $f$ the output terms, and $d$ are the direct feedthrough terms, which describes the effect of the higher frequency dynamics. The reduced form is obtained from experimental data by employing a structural fit such as the MATLAB function $ssest()$, and extracting the modal state-space matrices from the fit. These state-space terms are then utilized to define the low- and high-frequency asymptotes of the reduced plant:

$$P(\omega = 0) = \frac{1}{\omega_n^2} \begin{bmatrix} f_z b_w & f_z b_u \\ f_y b_w & f_y b_u \end{bmatrix} + \begin{bmatrix} d_{zw} & d_{zu} \\ d_{yw} & d_{yu} \end{bmatrix} \tag{6}$$

$$P(\omega = \infty) = \begin{bmatrix} d_{zw} & d_{zu} \\ d_{yw} & d_{yu} \end{bmatrix} \tag{7}$$

With these asymptote definitions, the $\gamma$ parameter can be defined, which describes the relation between the low- and high-frequency asymptotes:

$$\gamma_{ij} = \frac{P_{ij}(\omega = \infty)}{P_{ij}(\omega = 0) - P_{ij}(\omega = \infty)} = \begin{bmatrix} \gamma_{yu} & \gamma_{yw} \\ \gamma_{zu} & \gamma_{zw} \end{bmatrix} \tag{8}$$

Next, the $H_2$ and $H_\infty$ optimal PPF tuning problem can be solved using the determined $\gamma$-parameter. Both tuning methods yield similar controller gain, which is described as:

$$k_c = \frac{g}{1 + \gamma_{yu}} \frac{\omega_n^2}{f_y b_u} \tag{9}$$

The other controller parameters are described in Table VI.

TABLE VI: Optimal tuning parameters

| | $\omega_c/\omega_n$ | $\zeta$ |
|---|---|---|
| $H_2$ | $\frac{1}{\sqrt{1-g\frac{\gamma_{yu}-\gamma_{gw}-\gamma_{zu}}{1+\gamma_{yu}}}}$ | $\frac{1}{2}\sqrt{\frac{g}{1-g}\frac{1-g\frac{\gamma_{yu}-\gamma_{yu}-\gamma_{yu}-\gamma_{yu}}{1+\gamma_{yu}}}{1-g}}$ |
| $H_\infty$ | if $\gamma_{wy} = \gamma_{zu} = \gamma_{zw} = 0$ :<br>Polynomial approximation from Soltani et al. [11]<br>else:<br>Numerical continuation solution from Seinhorst et al. [4] | |

This optimal tuning method involves only one tuning variable, which is the static open-loop gain g, with the stability condition $g < 1$.

For a more analytical understanding of how these equations and parameters are defined, see [4].

## V. Materials and Experimental Design

This section elaborates on the preparation for the experimental phase. During this phase, prototype beams are manufactured with the piezo configuration based on section III, and the designs of the experimental setup are discussed.

### A. Test-setup

A test setup has been constructed to enable the beam to replicate the behavior of a cantilever beam with base excitation. Figure 21 shows the test setup for experimenting. The test-setup consists of a fixed steel block for clamping and a position sensor for measuring the tip displacement of the beam. Electrical wires are connected to the piezoelectric transducers to supply and read voltages. To generate external vibrations, a stack actuator is employed, which is integrated to the clamping system as illustrated in Figure 22. The stack actuator is clamped using a screw and functions as a base actuator to generate disturbance ($w$) in the cantilever beam. Figure 23 depicts the full schematic representation of the test-setup.

A Compact Rio receives and sends signals to the beam system. The shear piezoelectric element employed to actuate the system has an electric field of 1.5kV/mm, which means a maximum of 750V can be applied to the piezo actuator. Therefore, a high voltage amplifier Smart Materials $HVA1500/500$, with a gain of 200, is utilized to achieve the high voltages. However, this high voltage will not be experimented with due to safety reasons. The maximum voltage applied to the

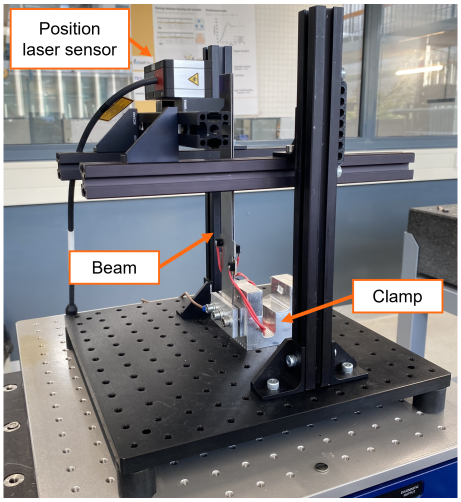


Fig. 21: Test setup

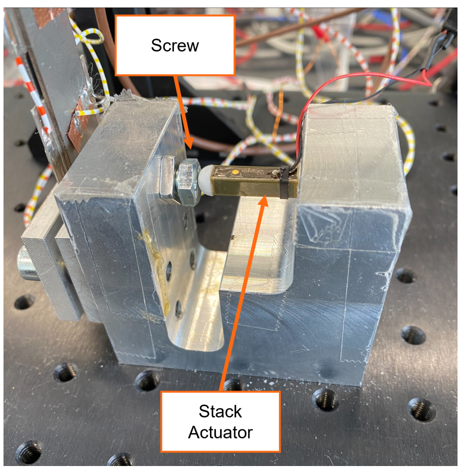


Fig. 22: Clamp with the integrated stack actuator for base vibration

piezo actuator is limited to ±250V. Additionally, a $Thorlabs$ $BPA100$ voltage amplifier is employed for the stack actuator. This amplifier has a lower gain and can go up to a minimum of -30V and a maximum of $150V$. The stack actuator requires a lower voltage than the shear piezoelectric actuator, and the limit set for this actuator is between 0 and 15V. Furthermore, a Kistler type 1008b charge amplifier is also utilized. Without a charge amplifier, the piezo sensor exhibits different behavior in magnitude and phase at low frequencies, which complicates control implementation. Therefore, a charge amplifier is employed to condition the output signals of the piezo sensor at these low frequencies. Appendix C further explains the necessity of having a charge amplifier.

### *B. Available beam materials and assembly*

The materials utilized for the beam's construction include stainless steel and shear piezoelectric elements manufactured by PI. The material of the obtained shear piezoelectric element plates is PIC255. The dimensions of these plates and the maximum electric field are shown in Table VII.

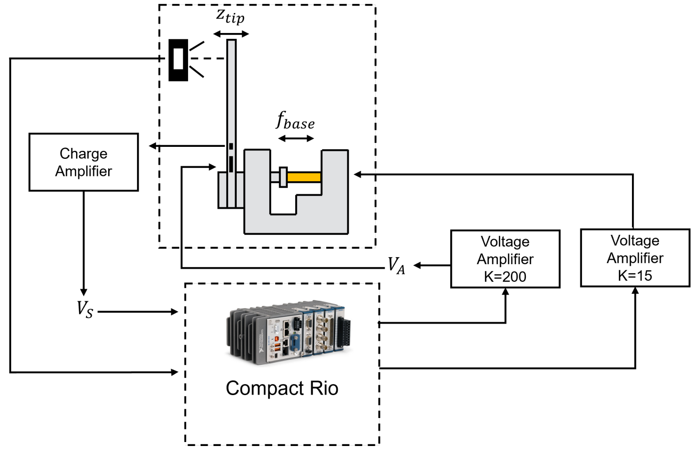


Fig. 23: Full schematic representation of the test setup

TABLE VII: PIC255 Shear Piezo plate

| parameter | Value | Unit |
|---|---|---|
| L (actuation direction) | 25 | [mm] |
| W | 25 | [mm] |
| H | 0.5 | [mm] |
| E | 1.5 | [kV/mm] |

To prevent issues such as short-circuiting, a method of integrating the shear piezoelectric elements into the beam design is required. One method is to fully isolate the piezoelectric element. However, additional insulation materials and epoxy glue need to be added. Therefore, the chosen method involves stacking two piezoelectric elements with different polarizations on top of each other, which results in the same shear. The positive terminal is positioned between the two piezoelectric elements, while the negative terminal and the ground are on the steel surface. This method also employs epoxy glue, but does not require additional insulation material. Figure 24 depicts the schematic of this approach. The method can be considered as a parallel system with the piezoelectric elements functioning as capacitors, and the steel plate with glue acting as resistors. Although epoxy glue is non-conductive, the glue layer is relatively thin. Consequently, the expectation is that the glue layer and the steel beam have zero resistance. Therefore, positioning the negative terminal and the ground on the steel plate is expected to drive the system.

### *C. Experimental design*

The goal is to manufacture the prototype design without sidewalls. The design must replicate the dynamic behavior of the system with sidewalls included. As analyzed in section III, the two proposed designs, with and without sidewalls, exhibit similar dynamic characteristics. Therefore, experimenting with the system without sidewalls provides a valuable starting point for understanding and predicting the behavior of the system with sidewalls included.

Furthermore, the optimal piezo configuration for the prototype beam is based on the findings from section III. Due to the availability of piezoelectric elements, the chosen piezoelectric element length is set at a maximum of 25mm. A potential

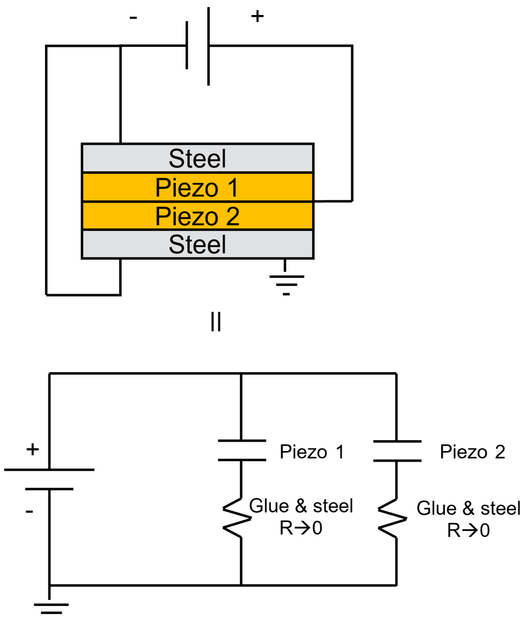


Fig. 24: insulation method explained in the electrical domain

solution to increase the actuation length is to stitch multiple actuators next to each other. However, this approach is not pursued to ease manufacturability. Moreover, the absence of sidewalls allows for an easier method of connecting the electrical wires to the system by misaligning the piezoelectric elements, as illustrated in Figure 25.

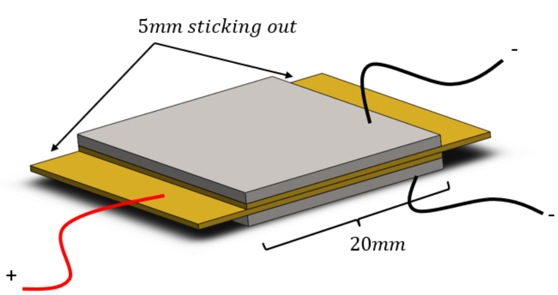


Fig. 25: Connectivity and insulation method

Due to the available piezo width of 25mm, the prototype width is reduced from 32mm to 20mm. Additionally, due to the stacking of the piezoelectric elements, the thickness of the core will increase from 0.5mm to 1mm. Table VIII presents the dimensions of the prototype beam.

TABLE VIII: Prototype beam dimension

| parameter | Value | Unit |
|---|---|---|
| L | 220 | [mm] |
| W | 20 | [mm] |
| H | 3 | [mm] |

*1) Non-Collocated design:* The piezo configuration for the proof-of-concept beam of the non-collocated beam is based on subsection III-B. According to this section, the optimal placement of the actuator is near the fixed end. For the proof-of-concept design, the actuator is positioned against the fixed end. The length of the actuator will be the maximum available length 25mm. Moreover, the gap between the actuator and the sensor is 10mm and the sensor length is also 10mm. The design is shown in Figure 26.

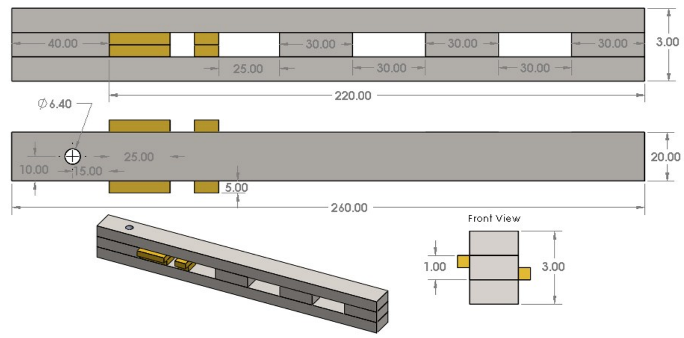


Fig. 26: Prototype non-collocated design

*2) Collocated design:* The second prototype design also has a piezoelectric element length of 25mm. The design is shown in Figure 27.

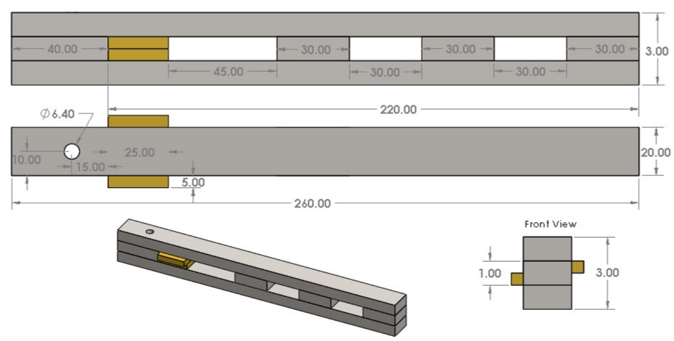


Fig. 27: Prototype collocated design

The chosen piezo configuration for the collocated piezo design is based on similar simulations as in subsection III-C. The values for the actuator width and sensor are shown in Table IX.

TABLE IX: Collocated piezo configuration

| parameter | Value | Unit |
|---|---|---|
| $w_a$ | 4 | [mm] |
| $w_s$ | 2 | [mm] |
| $w_{gap}$ | 5 | [mm] |

The values differ from those in subsection III-C due to the different dimensions of the prototype beam. However, the same method for determining the piezo configuration has been applied. The simulation process for determining the optimal piezo configuration for the prototype design is detailed in Appendix B. Furthermore, the structured electrode layer of the piezoelectric element is illustrated in Figure 28.

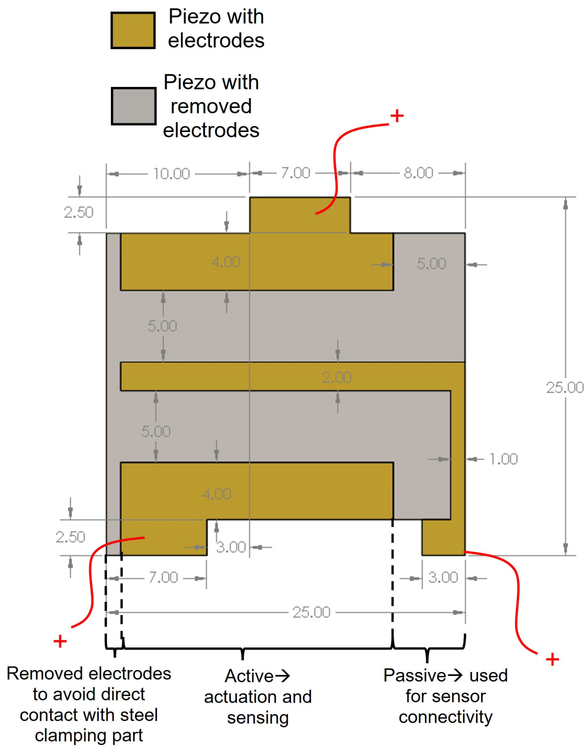


Fig. 28: Structured piezo for collocated configuration

The collocated piezo element consists of three parts. The first is the active part, which is utilized for actuation and sensing within the system. Additionally, there is a passive part that extends the sensor towards the open side of the beam to enable electrical connection. However, this results in a system that is not fully collocated. To achieve a fully collocated system, the passive component should be removed during optimization. Therefore, this design is considered to evaluate the potential of a structured electrode as a solution for vibration damping. The final part features a removed electrode edge to prevent direct contact with the steel clamping part, thereby avoiding short-circuiting.

## VI. Result and Discussion

This section discusses the results of the experiments. First, an open-loop identification is conducted. Based on the identified system, an optimal Positive Position Feedback (PPF) controller is designed and subsequently implemented in a second experiment to investigate whether control damping is applied.

### A. Open-Loop Identification of Non-Collocated Design

The manufactured beam with the non-collocated piezo configuration is depicted in Figure 29. The manufactured beam exhibits poor bonding of the piezoelectric elements. The lower piezoelectric element is well bonded to the lower beam, and the two stacked piezoelectric elements are bonded properly. However, the upper piezoelectric element is not effectively bonded to the upper beam, resulting in poor electrical connectivity and reduced shear actuation efficiency. To enhance

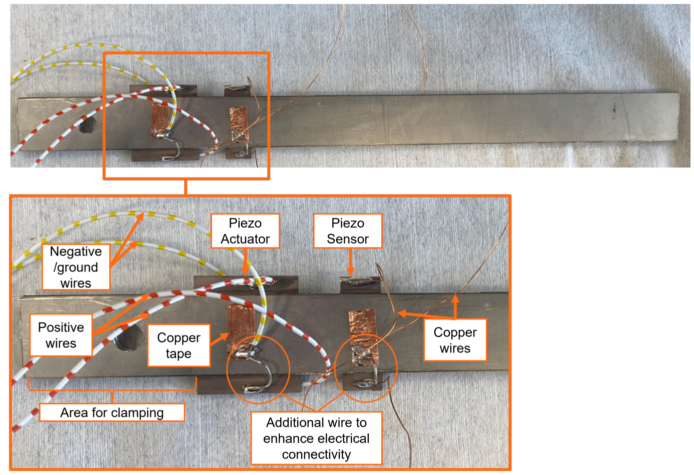


Fig. 29: Manufactured non-collocated prototype design

electrical connectivity, a wire is connected between the upper surface of the piezoelectric element and the top steel surface, as shown in this figure. Furthermore, it can be observed from the figure that copper wires are employed for the piezo sensors. Copper, known for its high conductivity, is utilized to improve electrical connectivity. Moreover, copper tape is employed to connect the ground wires to the beam's surface. Soldering the wires onto copper tape is more efficient than directly soldering onto steel. While it is possible to directly solder onto steel, additional steps are required to achieve this. The open-loop identification of this system is shown in Figure 30.

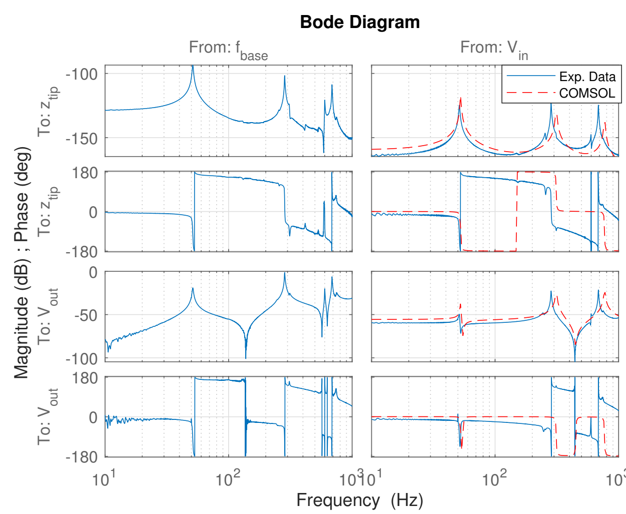


Fig. 30: Open-loop identification of the non-collocated system

The right column depicts the channels actuated by the shear piezoelectric actuator, while the left column depicts the channels actuated by the base actuator. The measured output of the channels actuated by the shear piezoelectric actuator is compared with the COMSOL simulation to validate the COMSOL model used in section III and the optimization method from section II. The measured results align well with the COMSOL simulation. However, there is a gain difference of approximately 5dB in the bodeplot $z_{\text{tip}}/V_{\text{in}}$, which might be due to the poor physical connection between the upper piezoelectric element and the top beam. The bodeplot $z_{\text{tip}}/V_{\text{in}}$ is also referred to as the actuator performance channel, as it is the bodeplot where the performance of the piezoelectric actuator can be observed. The values of the tip displacement of this channel are shown in Table X.

TABLE X: Non-collocated actuator tip displacement performance

| | Measured | | | |
|---|---|---|---|---|
| | Mode 1 | Mode 2 | Mode 3 | Required |
| Magnitude (dB) | -124.8 | -123.1 | -124.6 | -125.5 |
| Damping factor ($\zeta$) | 0.0084 | 0.0049 | 0.0043 | |

The damping factor for each mode is also presented and determined using the half-power bandwidth method [16]. The desired magnitude of tip displacement for a system with an electric field of 1.5kV/mm is at least $-125.5$dB. Below this magnitude, the system is capable of counteracting $400\mu$m tip displacement without becoming saturated. The current prototype has a measured tip displacement magnitude of $-124.8$dB for the first mode. Therefore, even with the gain drop, the prototype system is able to achieve the goal to actuate $400\mu$m. By reconstructing the COMSOL model based on the prototype design, and recreating the actuator length analysis plot from Figure 9, a prediction is made regarding the minimal length required to achieve $400\mu$m vibrations for the first mode. Figure 31 shows the recreated actuator length analysis plot based on the non-collocated prototype design.

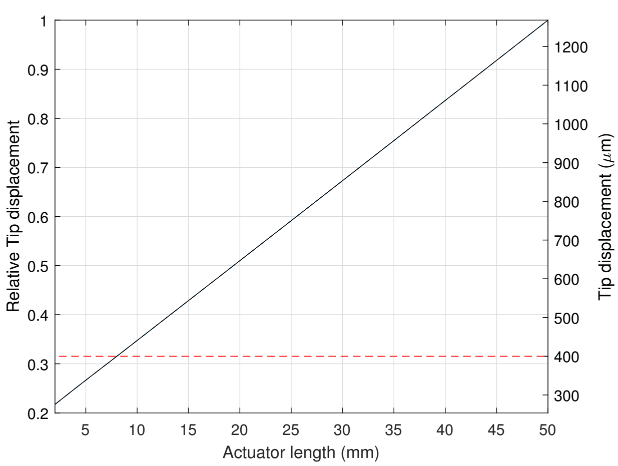


Fig. 31: actuator length analysis for the first mode. The left y-axis gives the tip displacement relative to the maximum performance. The right figure depicts the tip displacement output for the given non-collocated prototype system. The red dashed line represents the minimal required performance.

The plot shows a linear behavior, with the values relative to the maximum achievable performance. Knowing that the performance for an actuator length of 25mm is at $59\%$ of the maximum performance, the relative output values can be converted into tip displacement values for the given prototype system, as shown on the second y-axis of this figure. Assuming the gain drop of $+5$dB can be resolved and the magnitude at resonance frequency reduced to $-120$dB, a minimal actuator length of a 8mm is required to achieve $400\mu$m actuation.

Furthermore, the controller channel $V_{\text{out}}/V_{\text{in}}$ exhibits a decrease in phase over the frequency range, which could be problematic for control implementation. Due to the utilization of the PPF controller, which has a second-order roll-off effect, delay at higher frequencies should not be problematic. However, as observed from the bodeplot, there is slight delay around the first mode that could potentially cause stability issues for the PPF controller.

Lastly, when analyzing the base actuation channel $V_{\text{out}}/f_{\text{base}}$, a zero phase can be observed for an increasing slope at low frequencies. This is due to the charge amplifier, which functions as an inverting amplifier, introducing a 180-degree phase shift to the system.

### B. Closed-loop performance Non-Collocated Design

The PPF controller is designed based on section IV, and the initial step in designing this controller is to define the first mode's low- and high-frequency asymptotes for each channel to obtain the parameters of the models in equation (5) and (8). The structural fit to obtain these equations is shown in Figure 32. The optimality of the controller depends on the

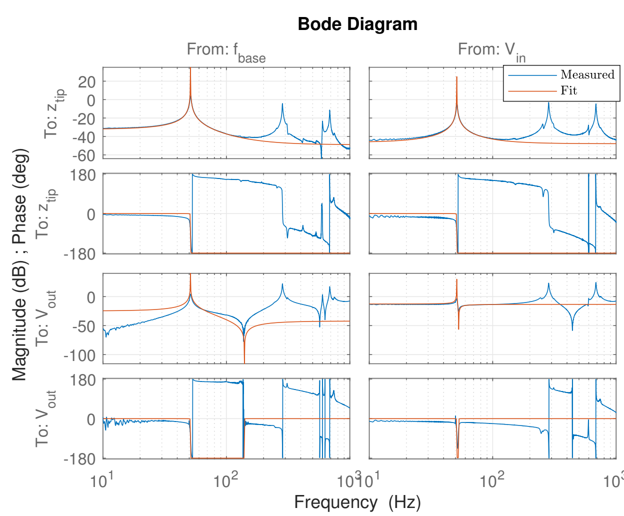


Fig. 32: Structured fit to obtain the reduced plant

quality of the fit. As seen from the figure, the fit matches relatively well, but is not perfect, particularly for the $V_{\text{out}}/f_{\text{base}}$ channel. With the $\gamma$-parameter identified, the optimal tuning parameters for the methods $H_2$ and $H_\infty$ can be determined. Using the optimal parameter values, the PPF controller is designed. The experimental results are shown in Figure 33.

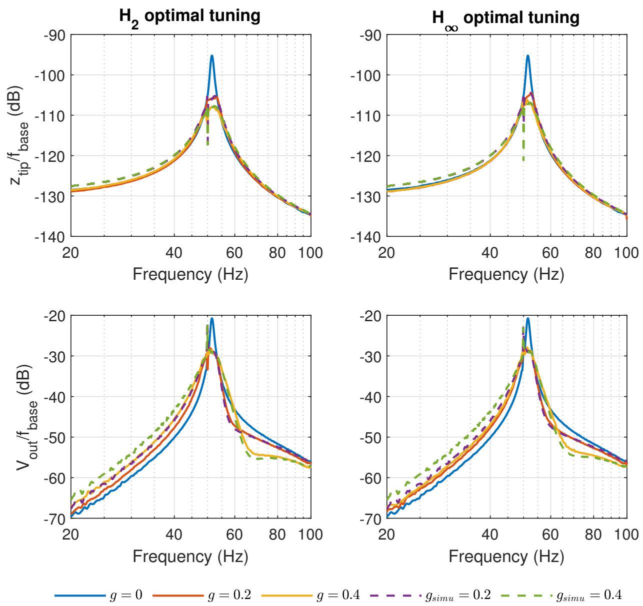


Fig. 33: Effect of the optimal PPF method on the non-collocated system. The dashed lines represent the theoretical closed-loop systems

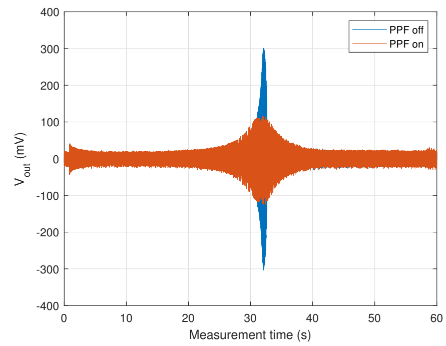


(a) $V_{\text{out}}$ output

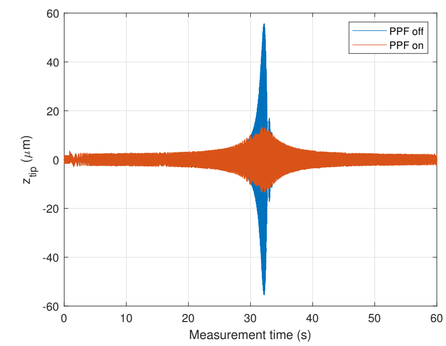


(b) $z_{\text{tip}}$ output

Fig. 34: A Frequency sweep up to 100 Hz for a time span of 60s is applied to the base actuation channel. The gain used for the PPF controller is g=0.4

This figure shows effective damping of the external vibrations for $z_{\text{tip}}$ and $V_{\text{out}}$. The main focus is to observe the damping performance of the tip displacement, as it is the key parameter of interest. Increasing the gain results in more effective damping of the tip displacement. According to section IV, the system remains stable if $g < 1$. However, the system becomes unstable when the gain exceeds $0.4$. The cause might be that there is still a slight phase lag around the first mode, which might limit the increase in gain. Appendix D further discusses the stability of the system through the analysis of Nyquist plots. Furthermore, Figure 34 depicts the damping result in time domain. This figure illustrates the effective damping provided by the controller in response to external vibration for $V_{\text{out}}$ and $z_{\text{tip}}$. At g = 0.4, the controller demonstrates significant damping for both outputs. For the output of interest $z_{\text{tip}}$, the controller is able to damp with $76.2\%$ from the original resonance peak. The system requirement is to suppress $400\mu$m external vibrations. From Table X, the voltage required to suppress $400\mu$m external vibrations is calculated as follows:

$$V_{\text{in}} = \frac{z_{\text{tip}}}{10^{(mag/20)}} = \frac{400\mu}{10^{(-124.8/20)}} \approx 695V$$

However, due to safety considerations, this high voltage is not applied during experimentation.

### C. *Open-Loop Identification of Collocated Design*

The following design is for a system with a collocated piezo configuration. Figure 35 depicts the manufactured system, and the structured piezoelectric element.

The piezoelectric element exhibits better adhesion to the steel surface compared to the non-collocated beam. Nevertheless, it is still not fully bonded. Additionally, the steel patches

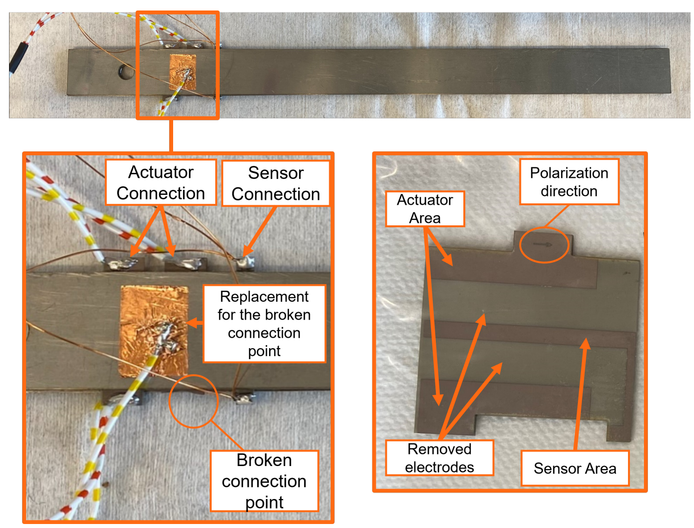


Fig. 35: Manufactured collocated prototype design, and the structured piezoelectric element

in the core layer are also poorly bonded. To optimize the electrical connectivity of the system, the negative terminals are positioned on the opposite side of each piezoelectric element as shown in this figure. However, as observed in this figure, a piece of the piezo connection point for the negative terminal is broken. Therefore, the negative terminal of this point is connected to the beam surface. Figure 36 depicts the open-loop identification of the system. When comparing the measured

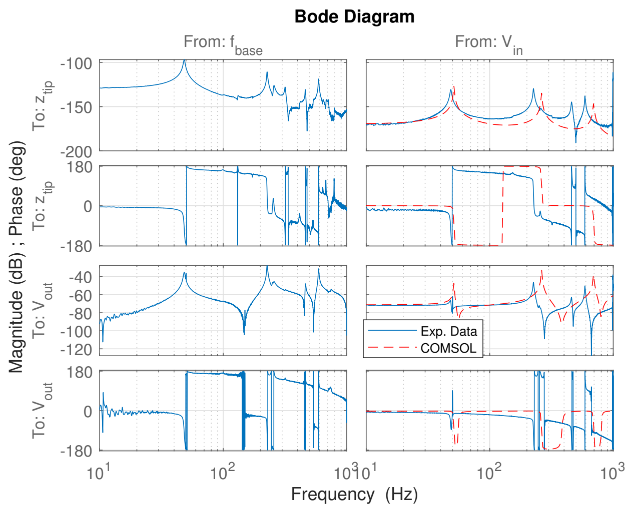


Fig. 36: Open-loop identification of the collocated system

bodeplot with the COMSOL simulation, it is observed that the measured system aligns relatively well until the second mode. The third mode appears to have split into two distinct modes. This could be due to the poor bonding of the piezoelectric element and the steel patches in the core layer, resulting in different dynamic behavior. Nevertheless, since the goal is to dampen the first mode of the system, this beam is still employed for further analysis. Next, the actuator performance channel is examined to determine whether the system meets the requirement of actuating $400\mu$m. The corresponding tip displacement resonance peak values are shown in Table XI.

TABLE XI: Collocated actuator tip displacement performance

| | Measured Mode 1 | Mode 2 | Mode 3 | Required |
|---|---|---|---|---|
| Magnitude (dB) | -130.8 | -129.6 | - | -125.5 |
| Damping factor $\zeta$ | 0.0119 | 0.0075 | - | |

As expected, the peak magnitude is lower than the magnitude of the non-collocated system due to the reduced actuator surface. The actuator performance of this system does not meet the required actuation performance. To meet this performance, the length of the actuator needs to be increased. Using a similar approach as in subsection VI-A, an actuator length analysis plot is recreated based on this prototype design, as shown in Figure 37. To achieve $400\mu$m actuation, an actuator length of 37.9mm is required.

The following observation from Figure 36 is the controller channel $V_{\text{out}}/V_{\text{in}}$. Similar to the non-collocated beam, an increase in phase lag over the frequency range is observed in the phase plot. Due to the utilization of a PPF controller, which has a second roll-off effect, the delay at higher frequency is not problematic for control implementation. Nevertheless, there is still some slight delay around the first mode which could cause stability issues for the controller.

### D. Closed-loop Collocated Design

Using the bodeplots from Figure 36, the optimal PPF controller can be designed. The structured fit to obtain the

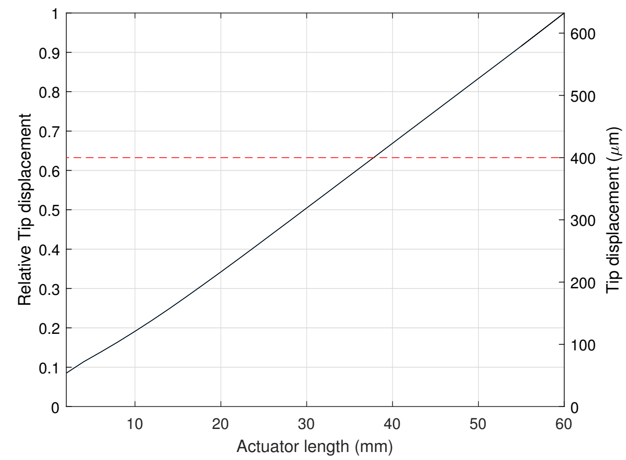


Fig. 37: actuator length analysis for the first mode. The left y-axis gives the tip displacement relative to the maximum performance. The right figure depicts the tip displacement output for the given collocated prototype system. The red dashed line represents the minimal required performance.

parameters of the model in equation (5) and (8) is shown in Figure 38.

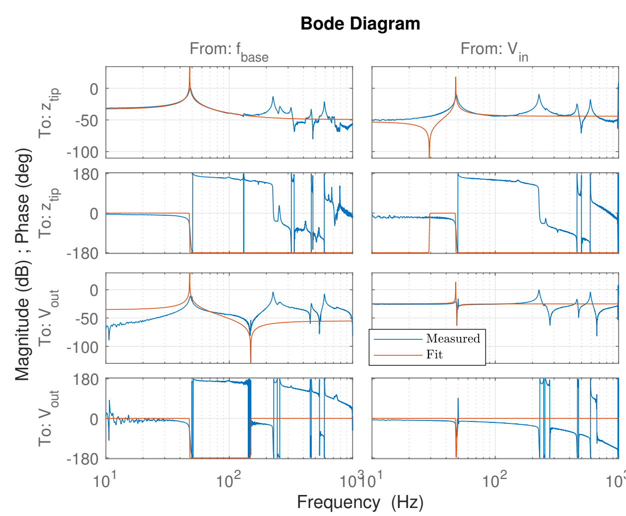


Fig. 38: Structured fit to obtain the reduced plant

Unlike the non-collocated design, achieving a good structured fit is more challenging. As observed in the actuator performance channel, the fit represents a different plant than the measured plant. The fit introduces a zero before the pole. Despite this limitation, a controller is designed based on these structured fits. With the $\gamma$-parameter determined from the structured fits, the optimal tuning parameters can be identified. The experimental result of the designed control is shown in Figure 39. Both PPF control with $H_2$ and $H_\infty$ norms show control damping for the performance channel $z_{\text{tip}}/f_{\text{base}}$. The base actuation channel $V_{\text{out}}/f_{\text{base}}$ shows minimal damping, which is due to the low resonance peak height in the controller channel limiting the damping performance. Although minimal damping is observed for the performance

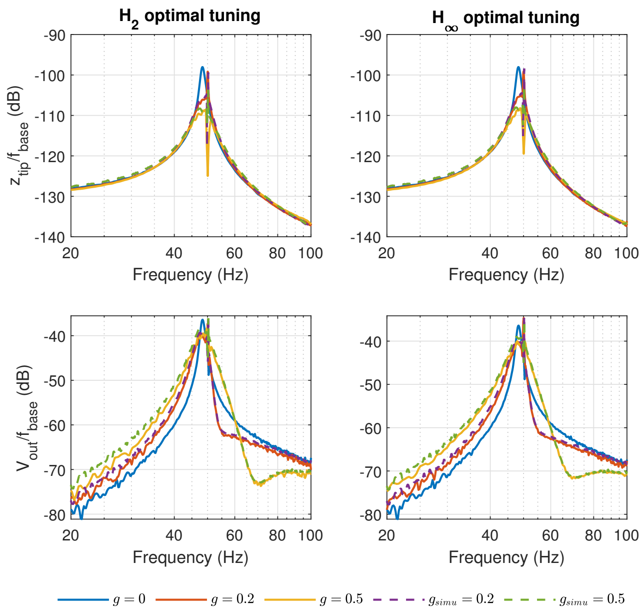


Fig. 39: Effect of the optimal PPF method on the collocated system. The dashed lines represent the theoretical closed-loop systems

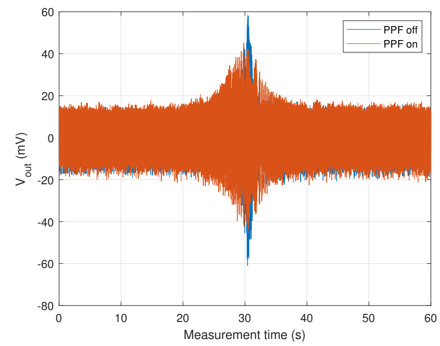


(a) $V_{\text{out}}$ output

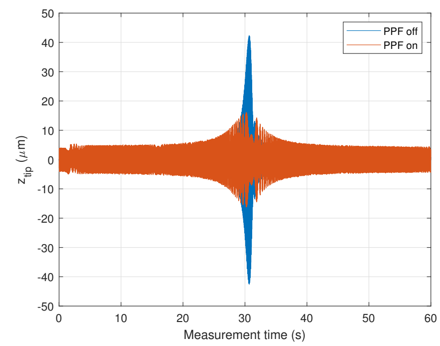


(b) $z_{\text{tip}}$ output

Fig. 40: A Frequency sweep up to 100 Hz for a time span of 60s is applied to the performance channel. The gain used for the PPF controller is g=0.5

channel $V_{\text{out}}$, more effective damping can be observed for the performance channel $z_{\text{tip}}$. This highlights the importance of of looking at the performance channel instead of other channels for tuning PPF. The maximum gain is at g=0.5. Increasing the value of the system makes it unstable, which might also be caused due to the delay. Appendix D discusses the stability of system further with Nyquist plots.

Furthermore, Figure 40 depicts the damping results in the time domain. Similar to the the bodeplot, the base actuation channel $V_{\text{out}}/f_{\text{base}}$ in time domain does not show an effective result in damping. Conversely, the performance $z_{\text{tip}}/f_{\text{base}}$ shows effective damping and is able to reduce the peak from the open-loop by $61.9\%$, which is significantly less than the performance of the non-collocated beam. This is attributed to the lower resonance peak height from the controller channel of the collocated beam compared to the non-collocated beam. The height difference, approximately 5dB, could cause the control performance difference.

## VII. Conclusion

Previous research conducted by Baken et al. [3] investigated a sandwich-structured beam with open sides and utilized foam in the core layer. In the final application, however, no foam can be utilized, and the sides must be enclosed to isolate the piezoelectric elements from external conditions. This research is a continuation of Baken's work and aims to further develop his beam design into an improved functional model for the ReMa blade system that has no core, includes sidewalls and is capable of suppressing $400\mu$m parasitic vibrations caused by the dynamic effect. To achieve the main goal of this research, the goal is divided into multiple subgoals:

1) Develop a conceptual design with sidewalls using the same dimensions as the current ReMa blade beam
2) Develop a prototype design that replicates the dynamic behavior of the design with sidewalls
3) Design a system capable of counteracting $400\mu m$ vibrations for the first fundamental mode
4) Achieve effective control damping for the first fundamental mode

The first subgoal is achieved by designing the system using COMSOL simulations. This design includes sidewalls with the same dimensions as the current ReMa blade system. To achieve the third subgoal for this system, the transverse displacement criterion proposed by Zhang and Sun et al. [5] and the EMCC method introduced by Trindade et al. [6] are employed to analyze the piezo configuration of the system capable of counteracting $400\mu$m tip vibrations.

From these piezo configuration methods, two designs are considered for further analysis: the non-collocated design and the collocated design. For demonstration, a prototype beam is designed that does not include sidewalls but replicates the system's dynamic behavior with side walls. This is achieved by placing multiple steel patches in the core layer. Simulations indicate that the prototype design closely resembles the behavior of the system with sidewalls. Therefore, this prototype design serves as a meaningful starting point for understanding and predicting the system's behavior with sidewalls. Furthermore, due to the piezos availability and the insulation method employed for electrical connections, the dimensions of the prototype slightly differ in width and thickness. However, these changes do not significantly affect the dynamics.

Once the prototype designs are manufactured, an open-loop identification is conducted to obtain a Bode plot with base ($f_{\text{base}}$) and shear actuation ($V_{\text{in}}$) as input and tip displacement ($z_{\text{tip}}$) and shear sensor ($V_{\text{out}}$) as output. From the actuator performance channel $z_{\text{tip}}/V_{\text{in}}$, the non-collocated beam is capable of actuating $400\mu$m without being saturated, thus achieving the third subgoal. Utilizing the transverse displacement criterion, the minimal required actuator length is predicted. The system suffers from performance loss due to poor manufacturing of the beam. Assuming this can be resolved, a minimal required length to achieve $400\mu$m actuation is $8.3$mm. For the collocated design, the system is not capable of actuating $400\mu$m. To achieve $400\mu$m actuation, the length of the piezo needs to be increased to $37.9$mm.

The next analysis is to check if control damping can be applied to the prototype system. The optimal controller method from Seinhorst et al. [4] is utilized to suppress the system's first fundamental mode. For the non-collocated configuration, the controller is able to damp $76.2\%$ of the first fundamental mode. For the collocated system, the controller is able to damp $61.9\%$, which is significantly less than the non-collocated design. The observed reduction in control performance may be attributed to the lower resonance peak height from the controller channel of the collocated beam compared to the non-collocated beam.

This research demonstrates how a conceptual design using sidewalls and the dimensions from the current ReMa blade can be designed to be capable of theoretically suppressing the $400\mu$m parasitic vibrations. However, the practical implementation of this design is not demonstrated. A prototype design is developed without sidewalls, yet it replicates the system's behavior with sidewalls. This prototype serves as a starting point for understanding and predicting the system behavior with sidewalls. Moreover, an optimal PPF controller is applied to this system, demonstrating effective damping of the first fundamental mode. These findings conclude how to design a beam system with sidewalls and show that the shear piezo can be utilized with a controller such as PPF to suppress parasitic vibrations.

## VIII. Recomendation and Future steps

This research presents promising results for achieving the ReMa blade system with integrated shear piezoelectric transducers for vibration damping. Nevertheless, the result can be further improved. This section discusses the possible improvements and further steps for achieving a final ReMa blade system capable of suppressing the parasitic vibrations.

### A. Improvements test setup

The current test setup yields satisfactory results for both open-loop identification and the implemented controller. However, the setup can be further optimized to achieve even better results. The main improvement that can be made is to reduce the delay in the controller channel $V_{\text{out}}/V_{\text{in}}$. The structured fit function for the optimal PPF controller is sensitive to delay, and the quality of the fit influences the controller's performance. Therefore, reducing the delay of the controller channel may improve the optimal PPF controller design further. A solution to this problem could be to use a lower resolution analog input. Decreasing the resolution, might lower the latency because the system requires fewer steps to digitize the analog signal. However, this proposed solution might induce noise. An alternative solution is to add phase lead to the system to compensate for the delay. This can be achieved using Smith Predictor Control [15].

### B. Improvements in beam manufacturing

The systems employed for experimental measurement suffer from poor glue bonding, which leads to a decrease in system performance. The main cause might be the thickness of the piezoelectric element that is not exactly equal to the thickness of the steel patches in the core layer. This prevents uniform contact between the piezoelectric element and the steel beam. Furthermore, an alternative method to consider is soldering the materials together rather than gluing them. This method has been attempted. However, soldering directly onto steel cannot be accomplished in one step. Multiple steps are required to achieve successful soldering on steel. If successful, this method may increase the bonding strength and conductivity of the system. For this research glue was employed instead to ease manufacturability.

### C. Improvements beam design

This research investigated both non-collocated and collocated designs. Both designs yield positive results. Nevertheless, both also have their advantages and disadvantages. The non-collocated design offers satisfactory performance, but an additional piezo sensor element is required, which takes up more space within the system. The collocated system is fully collocated, ensuring close loop stability. In this research, collocation is achieved by sharing the actuation and sensing space within a single piezoelectric element. However, to achieve the required actuation performance, the piezoelectric element length must be increased significantly. The limitations of both designs can be addressed by utilizing the self-sensing capabilities of the piezoelectric transducer. Jansen et al. [13] demonstrate how self-sensing in piezos is utilized for active damping purposes. This approach ensures a fully collocated system without the need for an additional piezoelectric element for sensing, and the piezoelectric element length does not have to increase significantly to meet the actuation requirement.

Furthermore, the next action is to place the piezoelectric element a bit further away from the fixed end because according to Figure 7, it might increase the actuator performance even more. This is not conducted in this research to simplify the manufacturing process. Also, the performance will not increase significantly, and it will be hard to confirm if it actually improves the system further in the real world. The other actions that can be conducted include implementing sidewalls to the system and analyzing the beam system in a horizontal orientation to move closer towards the system's application.

## References


[1] A Xihao Zhang, An Introduction to Lithography Machine, I Atlantis Press, pp. 49-53, 2021

[2] Yazan M. Al-Rawashdeh, Mohammad Al Janaideh, Marcel Heertjes, On characterization of a generic lithography machine in a multi-directional space, Mechanism and Machine Theory, vol. 170, pages 104638, 2022

[3] Mark Baken, Active Vibration Control of Sandwich Beam Structures utilizing internally placed Piezoelectric Shear Actuators and Sensors, Master thesis, University of delft, 2024

[4] Bram Seinhorst, Marijn Nijenhuis, Wouter Hakvoort, Gain Margin Constrained H2 and H Optimal Positive Position Feedback Control for Piezoelectric Vibration Suppression, SSRN: https://ssrn.com/abstract=5117631, 2024

[5] C T Sun, X D Zhang, Use of thickness-shear mode in adaptive sandwich structures, Smart Mater, vol. 3, pp. 202-206, 1995

[6] Marcelo A. Trindade, Ayech Benjeddou, Effective Electromechanical Coupling Coefficients of Piezoelectric Adaptive Structures: Critical Evaluation and Optimization, Mechanics of Advanced Materials and Structures, vol. 16, pp. 210-223, 2009

[7] Goksen G. Yaralioglu, Calculation and Measurement of Electromechanical Coupling Coefficient of Capacitive Micromachined Ultrasonic Transducers, Transactions on ultrasonics, ferroelectrics and frequency control, vol. 50, pp. 449-456, 2003

[8] Samer Abdelmoeti, Self-powered Vibration Control using Piezoelectric Materials in High Precision Machines, Master thesis, University of Twente, 2019

[9] Carlos Moutinho, Alvaro Cunha, Elsa Caetano Implementation of an active mass driver for increasing damping ratios of the laboratorial model of a building, University of Porto, Faculty of Engineering, Journal of Theoretical and Applied Mechanics, vol. 49, pp. 791-806, 2011

[10] Chuen jin Goh Analyisis and control of quasi distributed parameter systems, Thesis, California Intitute of Technology, Pasadena, CA, 1983

[11] P. Soltani, G. Kerschen, G. Tondreau, A. Deraemaeker Piezoelectric vibration damping using resonant shunt circuits: an exact solution, Smart Materials and Structures, vol. 23, pages 125014, 2014

[12] F. Coatto, Metastructures in a sensor-actuator configuration: the practical issues in bandgap generation, Master thesis, University of Delft, 2023

[13] B. Jansen, H. Butler, R. de Filippo Active Damping of Dynamical Structures Using Piezo Self Sensing, IFAC-PapersOnLine, vol. 52, pp. 543-548, 2019

[14] A. Den Hamer, G. Z. Angelis, and N. Roozen, Broad-band active vibration suppression using ppf focused on industrial application, IEEE/ASME Transactions On Mechatronics, vol. 10, pp. 146–153, 2005

[15] Abe, Naoto and Yamanaka, Kazuo, Smith Predictor Control and Internal Model Control, Proceedings of SICE 2003 Annual Conference, pp. 1383-1387, vol. 2, 2003

[16] Papagiannopoulos, George and Hatzigeorgiou, George, On the use of the half-power bandwidth method to estimate damping in building structures, Soil Dynamics and Earthquake Engineering - SOIL DYNAM EARTHQUAKE ENG, vol. 31, pp. 1075-1079, 2011,


## Appendix A
## Sytem with and without sidewalls

The optimization of the prototype design is based on the optimization method from section III. The optimization described in this section is conducted with a model that includes sidewalls. For the prototype design, the sidewalls are not included. Nevertheless, steel patches are integrated into the system which resemble the dynamics of a system with sidewalls. This section discusses the comparison of the system with and without sidewalls based on the ReMa blade dimension from Table I. The comparison is conducted using a non-collocated piezo configuration, where the actuator, 30mm in length, is placed against the fixed end, and a piezoelectric sensor, 10mm in length, is placed 10mm from the actuator. The bodeplots of $z_{\text{tip}}$ and $V_{\text{out}}$ against $V_{\text{in}}$ are shown in Figure 41.

As depicted in the bodeplot $z_{\text{tip}}/V_{\text{in}}$, the designs with and without the sidewalls exhibit a similar behavior. Thus, the additional sidewalls do not significantly alter the system's transverse placement. Moreover, the bodeplot $V_{\text{out}}/V_{\text{in}}$ is also similar, but it exhibits a notable gain difference. Additionally, the sidewalls appear to have a positive impact on the wider spacing between the resonance and antiresonance, making control implementation significantly easier. Figure 16 shows that varying sensor length may have a positive impact on widening the resonance and antiresonance of the mode. Unlike the system with sidewalls, the system without sidewalls has no positive effect on the system, as shown in Figure 42. It appears that increasing the length results in lower coupling, and the resonance and antiresonance of each mode do not widen significantly. Hence, for the prototype design, the sensor is positioned at 10mm to maintain high coupling and achieve better near-collocated behavior. Additionally, the pole and zero of the first mode of both systems are closely spaced. Therefore, experiments will be performed to determine if effective control damping can be achieved for a system with closely placed poles and zeros.

Thus, the design with the chosen piezo configuration closely resembles the system with sidewalls in terms of dynamic behavior. Therefore, using this system for the initial prototype serves as a good starting point for understanding and

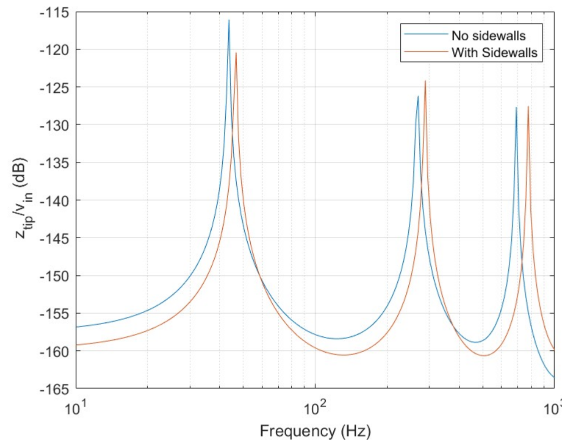


(a) $z_{\text{tip}}/V_{\text{in}}$

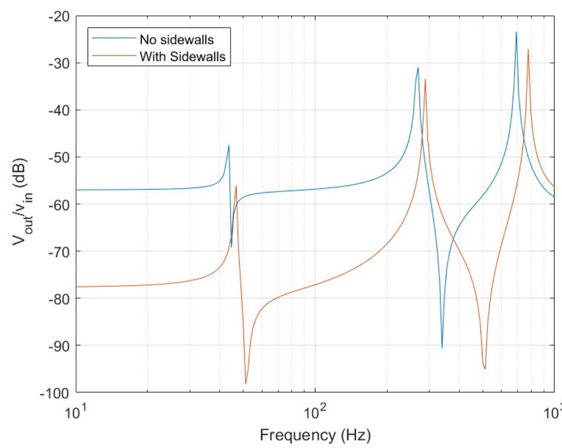


(b) $V_{\text{out}}/V_{\text{in}}$

Fig. 41: Comparison with and without sidewalls

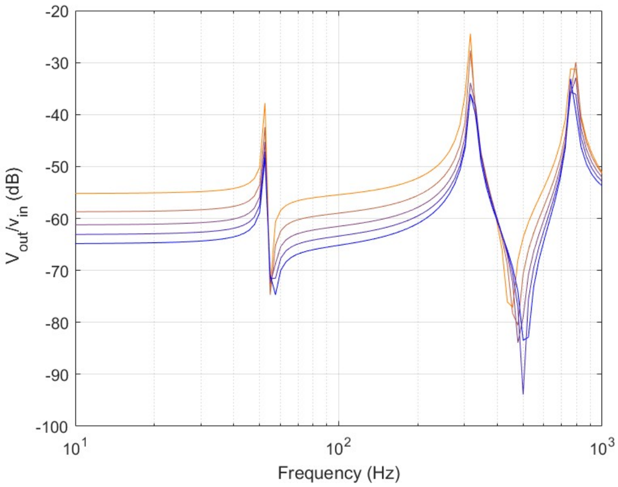


Fig. 42: Bodeplots of multiple variable sensor length for a system without sidewalls starting from yellow 5mm to blue 20mm

predicting the behavior of the system with sidewalls.

## APPENDIX B
## PROTOTYPE COLLOCATED DESIGN

subsection III-C discussed the optimal actuator, sensor, and gap width for the collocated piezo configuration. However, the values for the prototype design, except for the sensor width, differ due to the different beam dimensions. Hence, this section focuses on determining the optimal piezo configuration for the collocated prototype design. Figure 43 shows the DC value of $V_{\text{out}}/V_{\text{in}}$ against actuator width. The figure shows a similar

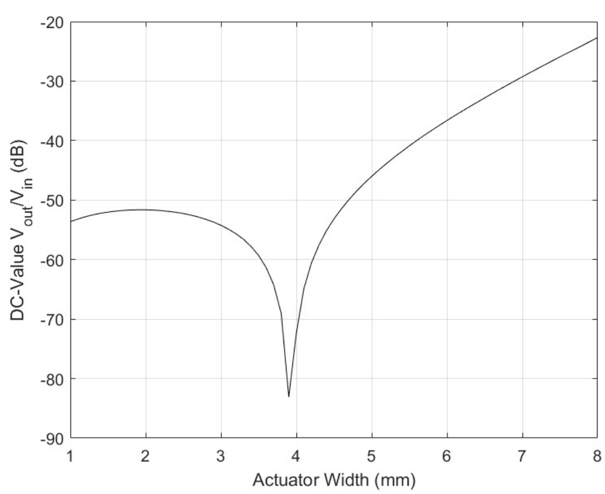


Fig. 43: DC value of $V_{\text{out}}/V_{\text{in}}$ against actuator width for the prototype beam

behavior as in Figure 18. Figure 44 depicts what the bodeplots look like when the actuator width is on the left side and right side of the minimum. Figure 44b has an antiresonance before the first mode resonance, whereas Figure 44a does not. In Figure 44b, the DC coupling will increase as the actuator

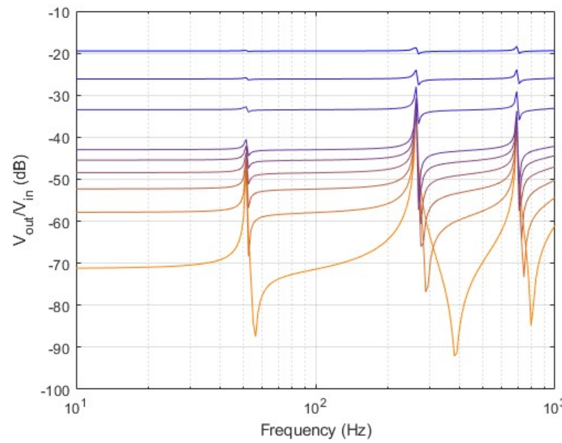


(a) Bodeplots starting from yellow 4mm to blue 8mm actuator width

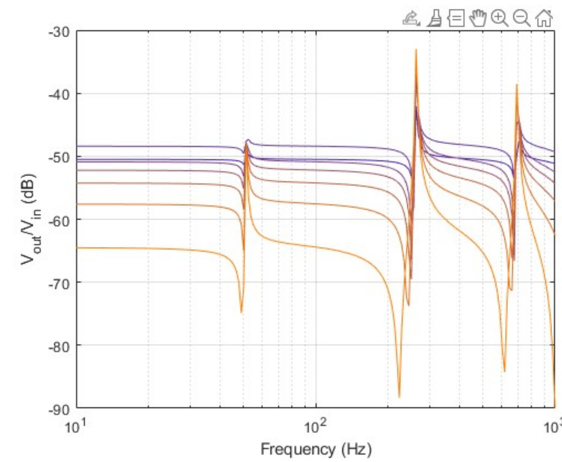


(b) Bodeplots starting from yellow 3.8mm to blue 1mm actuator width

Fig. 44: bodeplots from Figure 43

width decreases further. However, the resonance height will also decrease, which will limit control implementation. For the prototype design, focusing more on Figure 44a makes more sense, as actuation performance needs to be as high as possible. Among these piezo configurations, an actuator width is selected that provides sufficient actuation while supporting effective control implementation. Hence, an actuator width of 4mm is chosen for the prototype design.

## APPENDIX C
## SYSTEM COMPONENTS

### A. *Micron-Epsilon Opto NCDT-1900-2 triangulator sensor*

The Micron-Epsilon Opto NCDT-1900-2 triangulator sensor is employed to measure the tip displacement of the system. This specific laser is capable of measuring displacements in micrometers, with a maximum displacement of 2mm. These specifications are essential to detect the range of motion of the system. During measurement, the position laser is set at the maximum sample frequency $f_s$ of 7.5kHz. Setting the $f_s$ at its maximum minimizes the system's delay, which gives a better fit to obtain the reduced plant for the optimal PPF controller. The position laser sends out voltages in the range between 0 and 10V. The output voltages are proportional to position displacement. The relation is defined as:

$$x_{me} = V_{me}\frac{x_{max}}{V_{max}} = V_{me}\frac{2}{10} \tag{10}$$

$V_{me}$ is the measured voltage in V and $x_{me}$ is the measured displacement output in (mm).

### B. Charge Amplifier

The piezoelectric transducers can be modelled as a capacitor in parallel with an internal resistance. When connecting the piezoelectric elements directly to the measurement system, which also has an internal resistance, it creates an RC high-pass filter effect with a characteristic cut-off frequency. This effect can be undesired for measurement purposes, as it could introduce a phase lead, which complicates control implementation. To address this, a charge amplifier is employed to lower the cutoff frequency, thereby improving the signal at lower frequencies. In the experimental test setup, a Kistler type 1008b charge amplifier is utilized for measurement. With this charge amplifier, the lower cut-off frequency can be tuned, and also the high cutoff frequency for the low-pass filter.

### C. Data acquisition system

The Compact Rio is utilized for sending and receiving signals. This Hardware is necessary because of the FPGA. An FPGA is a reprogrammable integrated circuit that allows custom logic. The primary feature of the FPGA is its low latency. The low latency minimizes the delay in the system, which is important for control implementation. The Compact Rio comes with the modules:

- NI 9263 Analog output
- NI 9205 Analog Input

Both modules are 16-bit, allowing for accurate readings within the system's range of motion. The compact Rio, along with its accompanying modules, operates with LabVIEW. The utilized code to run the system is developed by Coatto. A detailed description of his code, can be found in [12] .

## Appendix D
## Nyquist Stability Analysis

The results presented in section VI discuss the optimal PPF controller performance on the collocated and non-collocated systems. The stability condition for the controller is $g < 1$. However, it was concluded that at a certain point, the gain led to unstable behavior even though it should be stable according to the stability condition. This section shows the Nyquist plots for the measured non-collocated system with the theoretical $H_2$ optimal PPF controller and shows how these plots evolve as the gain increases. Figure 45 depicts the Nyquist plots for three gain values.

At $g = 0.4$, the system remains stable as the Nyquist curves do not encircle the critical point at $-1$ for all plots. In practice, this system also demonstrated stability and achieved significant

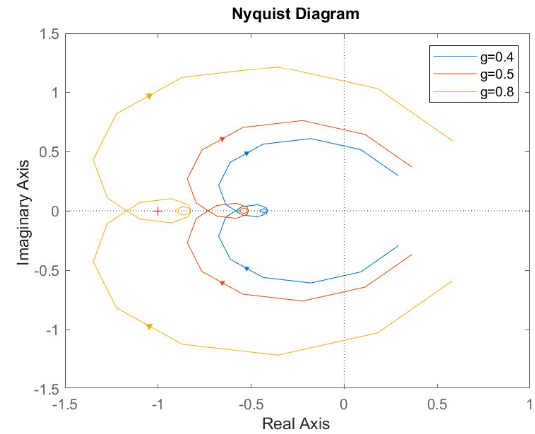


(a) Analysis of System Dynamics up to 1 Hz

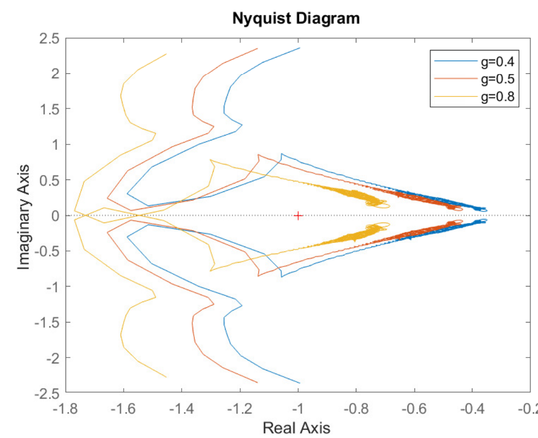


(b) Analysis of System Dynamics between 10 and 51 Hz

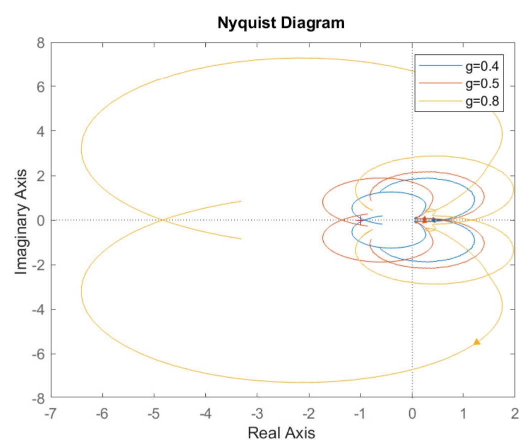


(c) Analysis of System Dynamics btween 60 and 287 Hz

Fig. 45: Nyquist plots for Non-collocated system using the $H_2$ PPF control

damping. However, when the gain is increased to $g = 0.5$, the system becomes unstable in practice. This, is shown back in Figure 45c. At approximately 286Hz, which corresponds to the second resonance frequency, the system with this gain encircles the critical point, leading to instability. For $g = 0.8$, instability already starts at low frequencies, as shown in

Figure 45a. These instabilities are primarily attributed to the time delay introduced in the system.

## Appendix E
## Shear stress analysis

This section discusses why the actuator and sensor should be located near the fixed end and the node points of the mode shape for optimal placement. Figure 46 depicts the mode shapes of the cantilever system. As you can see, the node points can be found at 170mm for the second mode and 110mm and 280mm for the third mode. Next, an analysis is conducted using the simulation based on subsection III-B, where the sensor of a non-collocated beam is varied along the length of the beam. In the COMSOL simulation, the average shear stress on the sensor element is measured and plotted against sensor position, see Figure 47. The graph shows a similar result to that in Figure 12. It can be confirmed that high shear stresses occur near the fixed end and at node points, while low stresses are observed at anti-nodes when the system is subjected to vibrations. Additionally, inducing shear stresses at this point will lead to higher vibrations. Therefore, placing this actuator or sensors at these places will enhance their performance, explaining the graph behavior of Figure 12 and Figure 7.

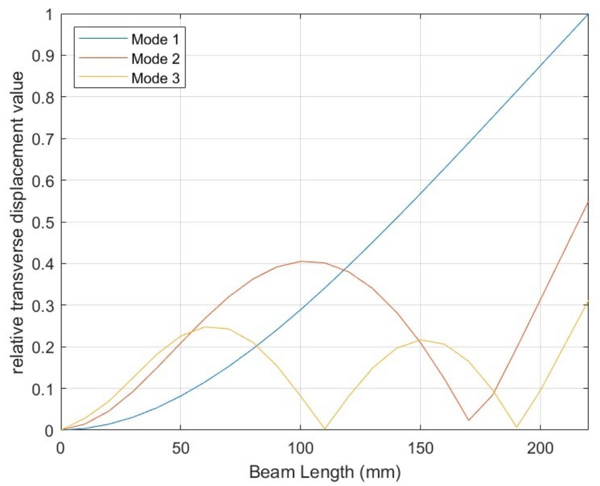


Fig. 46: mode shape of the cantilever beam system with sidewalls

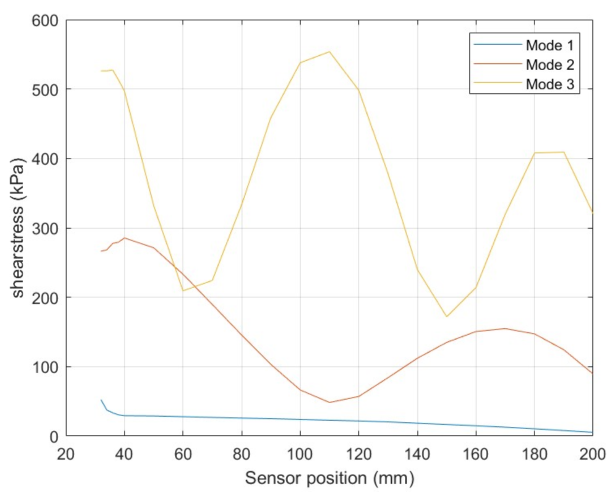


Fig. 47: Average shearstresses on the sensor against sensor position

## Appendix F
## Baken's Beam

The main goal of this research if to further develop Baken's beam through a proof of concept beam that represents closer to the ReMa blade system capable of damping the parasitic vibrations. The beam that is utilized by Baken at al. [3] is shown in Figure 48.

(a) Front view of Baken's beam

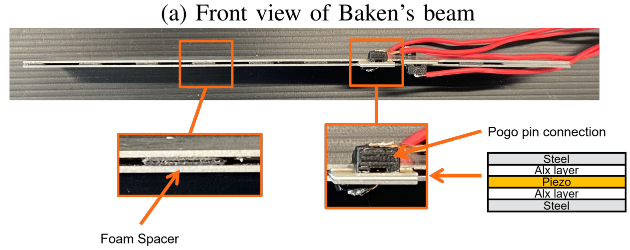


(b) Sideview of Baken's beam.

Fig. 48: Prototype beam utilized in Baken's research [3]

This beam employs foam spacers in the core layer, resulting in a system with low stiffness. Due to the presence of foam spacers, the dynamics and the piezo configurations differ from those of the conceptual beam with sidewalls and the prototype beam, which uses steel patches instead of foam in the core layer.

Furthermore, the manufacturing approach for the beam is also different. His beam utilizes pogo pins to enhance electrical connectivity, and employs a different insulation method compared to the prototype manufactured in this research. His imsulation method involves fully isolating the piezoelectric element using alumina (Alx) layers to prevent direct contact with steel and thus avoid short circuiting.